

1 **Measurement report: Optical properties of carbonaceous aerosols modulated by source**  
2 **variations of spring haze**

3 Yuan Cheng<sup>1</sup>, Jiu-meng Liu<sup>1,\*</sup>, Xu-bing Cao<sup>1</sup>, Yang-mei Guo<sup>1</sup>, Ying-jie Zhong<sup>1</sup>, Zhi-qing Zhang<sup>1</sup>,  
4 Ke-bin He<sup>2</sup>

5 <sup>1</sup> State Key Laboratory of Urban-rural Water Resource and Environment, School of Environment,  
6 Harbin Institute of Technology, Harbin, 150090, China

7 <sup>2</sup> State Key Laboratory of Regional Environment and Sustainability, School of Environment,  
8 Tsinghua University, Beijing 100084, China

9 Corresponding author. Jiu-meng Liu (jiumengliu@hit.edu.cn).

10 **Abstract**

11 Carbonaceous aerosols exert unique impacts on earth energy balance, but are not well constrained  
12 in air quality and climate models yet. In this study, a field campaign was conducted in a [Chinese](#)  
13 [megacity](#) ~~Northeast China~~ during a spring season to explore the optical properties of carbonaceous  
14 aerosols modulated by dramatic variations of particulate matter sources. We first integrated the light  
15 absorption results derived from different methods, including both on-line and off-line approaches.  
16 Then by synthesizing a series of source-relevant signatures, three types of haze episodes were  
17 identified. In general, agricultural fire emissions exerted strong influences on brown carbon (BrC),  
18 by effectively increasing the mass absorption efficiency (MAE) of bulk BrC, and emitting  
19 chromophores with a characteristic absorption peak at ~365 nm. Specifically, fires with low  
20 combustion efficiencies were more capable of enhancing the impacts of BrC on bulk aerosol  
21 absorption, and were more favorable for the emissions of organic compounds with relatively high  
22 molecular weights and aromatic contents. In addition, the agricultural fires, especially those with  
23 relatively low efficiencies, resulted in overestimations of black carbon (BC) mass by thermal-optical  
24 method due to unique emitted species. [BC concentrations were also overestimated for the dust](#)

25 [episodes](#). By excluding the impacts from agricultural fires and dusts, we unfolded the influence of  
26 secondary aerosol formation on the MAE of BC ( $MAE_{BC}$ ). With the enhancement of secondary  
27 aerosols,  $MAE_{BC}$  was found to exhibit a clear increasing trend, which could be translated into the  
28 light absorption enhancement ( $E_{abs}$ ) factors of up to  $\sim 2.3$ .

## 29 1. Introduction

30 Carbonaceous aerosols, which consist of organic compounds and black carbon (BC), exert  
31 unique impacts on earth energy balance (Bond et al., 2013), e.g., through absorbing and scattering  
32 solar radiation, influencing cloud processes, and deposition on ice and snow cover. However, as a  
33 complex mixture of compounds with continuing changes in chemical and physical properties  
34 (Pöschl, 2005; Andreae and Gelencsér, 2006), carbonaceous aerosols remained poorly constrained  
35 in air quality and climate models. For example, challenges still existed in the simulation of the  
36 sources, abundances, optical properties and radiative forcing of BC (Samset et al., 2014; Winiger et  
37 al., 2019; Gao et al., 2022; Chen et al., 2025; Wang et al., 2025). Similarly, discrepancies in the  
38 modeled and observed results were also evident for organic aerosol (OA), e.g., as indicated by the  
39 difficulties in proper predictions of [several key fractions including](#) primary OA emitted by open  
40 burning (Zhong et al., 2023), secondary OA (SOA) formed by volatility organic compounds (VOCs)  
41 with relatively low saturation vapor concentrations (Chang et al., 2022), and light absorbing OA,  
42 i.e., brown carbon (Tuccella et al., 2025). On one hand, state-of-the-art models were subject to  
43 various uncertainties such as those associated with the emission inventories, the treatments of BC  
44 lifetime and mixing state, the formation pathways of SOA, and the parameterization of brown  
45 carbon. On the other hand, there were also uncertainties in the observational results of carbonaceous  
46 aerosols. For example, measured BC were frequently found to differ by several times among various  
47 detection approaches (~~Tinorua et al., 2024~~) [such as the thermal-optical \(e.g., carbon analyzer\), light](#)  
48 [absorption \(e.g., Aethalometer\) and laser-induced incandescence \(e.g., single-particle soot](#)  
49 [photometer\) ones \(Tinorua et al., 2024\).](#) These techniques are mainly based on the high thermal-  
50 [stability, strong light-absorbing, and refractory properties of black carbon, respectively, while none](#)

51 of them has been established as a reference method (Petzold et al., 2013). In addition, it was  
52 commonly believed that inter-method differences in BC results were closely related to aerosol  
53 sources, but the influencing factors at play were not well understood (Pileci et al., 2021). Thus,  
54 largely constrained by the multitude of measurement principles, it remained challenging to integrate  
55 the observational and the subsequent interpretation (e.g., source apportionment) results on  
56 carbonaceous aerosols across studies and regions (Putaud et al., 2025).

57 In China, the ambient fine particulate matter (PM<sub>2.5</sub>) pollution has been reduced substantially  
58 since 2013 (Geng et al., 2024), ~~driven by a series of national-level policies including the *Action Plan*~~  
59 ~~*for Air Pollution Prevention and Control (2013–2017)*, the *Three-Year Action Plan for Winning the*~~  
60 ~~*Blue Sky Defense Battle (2018–2020)* and the *Action Plan for Continuous Improvement of Air*~~  
61 ~~*Quality (2023–2025)*. More recently, a new round of revisions for the Ambient Air Quality~~  
62 ~~Standards were launched by the Ministry of Ecology and Environment (MEE) of China, e.g., the~~  
63 ~~Class 2 standards of PM<sub>2.5</sub> will be tightened from 35 to 25 µg/m<sup>3</sup> for annual average and from 75 to~~  
64 ~~50 µg/m<sup>3</sup> for 24-hour average (National Public Service Platform for Standards Information, 2025).~~  
65 More recently, the Ministry of Ecology and Environment (MEE) of China released stricter Ambient  
66 Air Quality Standards for PM<sub>2.5</sub> (MEE, 2026), e.g., starting from 2031, the Class 2 standards will  
67 be reduced to 25 from 35 µg/m<sup>3</sup> for annual average (with an interim limit of 30 µg/m<sup>3</sup> for 2026–  
68 2030) and to 50 from 75 µg/m<sup>3</sup> for 24-hour average (with an interim limit of 60 µg/m<sup>3</sup>). The revised  
69 new standards, ~~which are expected to be officially released soon~~, provide new additional impetus  
70 for air quality improvement and meanwhile place great demands on a stronger observational support  
71 for PM<sub>2.5</sub> pollution control. This is particularly the case for Northeast China, which was overlooked  
72 by all of the ~~three~~ national-level action plans implemented during 2013–2025 and showed relatively

73 slow decreasing rate of PM<sub>2.5</sub> (Xiao et al., 2022).

74 Northeast China comprises three provinces (i.e., Liaoning, Jilin and Heilongjiang) and involves  
75 two national-level city clusters, i.e., Harbin-Changchun (HC) and Central-Southern Liaoning.  
76 Among the two city-cluster regions, HC differs more significantly from the traditional hotspots for  
77 air pollution control, e.g., Beijing and the surrounding areas. The distinctiveness of HC could be  
78 seen from two aspects (Cheng and He, 2026). First, HC is located in a severe cold climate region  
79 (e.g., with a seasonal average of  $-15$  °C in Harbin's winter), leading to intensive energy use in the  
80 cold winters for heating and thus high emissions of anthropogenic pollutants. Second, HC is within  
81 a major agricultural region, where open burning of crop residues remains prevalent after autumn  
82 harvesting and before spring planting in the next year. The agricultural fires frequently resulted in  
83 heavy pollution episodes, e.g., with record-high PM<sub>2.5</sub> concentration of  $\sim 2350$   $\mu\text{g}/\text{m}^3$  (1-hour  
84 average) in Harbin (Cheng et al., 2021). Despite the distinct emission system sources, the aerosols  
85 in HC (e.g., regarding their chemical compositions, source contributions, optical properties and  
86 impacts) have not been comprehensively explored, as indicated by the limited number of studies  
87 available (e.g., Wu et al., 2020; Zhang et al., 2020; Xie et al., 2024).

88 By combining on-line and off-line measurements, a field campaign was conducted in the  
89 central city of HC during a period with dramatic variations of aerosol sources and compositions.  
90 From a technical perspective, we elucidated the inter-method discrepancies in light absorption  
91 coefficients of carbonaceous aerosols, including both black and brown carbon. From a scientific  
92 perspective, we highlighted the signatures of various types of episodes and unfolded the responses  
93 of aerosol optical properties to agricultural fire emissions and secondary aerosol formation. We also  
94 demonstrated that nocturnal nitrate formation could be effectively enhanced by agricultural fires,

95 and thermal-optical measurement of BC mass could be subject to substantial artifacts during specific  
96 episodes. This study provided insights into the links between optical and chemical properties of  
97 aerosols in Northeast China, which are essential for understanding the haze pollution in this distinct  
98 but largely unexplored region.

## 99 **2. Methods**

### 100 **2.1 On-line observations**

101 Aerosol optical properties and mass concentrations of gaseous pollutants were measured with  
102 high time resolutions for about one month (from April 1 to May 2, 2023) in Harbin. The observation  
103 was performed on the campus of Harbin Institute of Technology (HIT), an urban site surrounded by  
104 residential and commercial areas. For aerosol measurements, ambient air was drawn into a stainless-  
105 steel sampling line at a flow rate of 16.7 L/min, using a vacuum pump (VACUUBRAND, Wertheim,  
106 Germany) and a mass flow controller (Alicat Scientific Inc., AZ, USA). After passing through a  
107 PM<sub>2.5</sub> cyclone (URG-2000-30EH; URG Corp., NC, USA) and a Nafion dryer (MD-700; Perma Pure  
108 LLC, NJ, USA), the sampled aerosols were measured by a photoacoustic extinctionsmeter (PAX;  
109 Droplet Measurement Technologies LLC, CO, USA) and a dual-spot Aethalometer (AE33; Aerosol  
110 d.o.o., Ljubljana, Slovenia). The PAX was operated at a wavelength ( $\lambda$ ) of 870 nm based on *in-situ*  
111 measurement approaches, i.e., photoacoustic method for the light absorption coefficient ( $b_{\text{abs}}$ ) and a  
112 wide-angle integrating reciprocal nephelometer for the scattering coefficient ( $b_{\text{scat}}$ ). The single  
113 scattering albedo (SSA) was calculated as the ratio of  $b_{\text{scat}}$  to extinction coefficient ( $b_{\text{ext}}$ , the sum of  
114  $b_{\text{abs}}$  and  $b_{\text{scat}}$ ). While the *in-situ* approach of PAX was used as the reference method for light  
115 absorption measurements, ~~In addition,~~ the AE33, which was operated with M8060 filter tapes,  
116 provided aerosol absorption coefficients at seven wavelengths (i.e., 370, 470, 520, 590, 660, 880

117 and 950 nm). It has been widely acknowledged that filter-based absorption measurement could be  
118 biased by the loading effect and the multiple scattering effect (Weingartner et al., 2003; Collaud  
119 Coen et al., 2010). For AE33, the former had been accounted for by a compensation algorithm based  
120 on absorption measurements from two differently loaded filter spots (Drinovec et al., 2015), while  
121 the latter was typically corrected using an empirical parameter ( $C$ ). The manufacture recommended  
122 a constant of 1.39 for  $C$ , but the experimentally determined  $C$  values were frequently found to  
123 deviate considerably from the suggested value, with tempo-spatial variations and dependences on  
124 aerosol properties (Ferrero et al., 2021; Yus-Díez et al., 2021, 2025; Renzi et al., 2026). In this study,  
125 the default multiple scattering correction (assuming  $C = 1.39$ ) was not applied and the corresponding  
126 absorption coefficients, which had only been corrected for the loading effect, will be specified as  
127  $(b_{\text{abs}})^*$ . Refer to Supplement for a more detailed description of  $(b_{\text{abs}})^*$ . The aerosol absorption  
128 Ångström exponent ( $\text{AAE}_{\text{bulk}}$ ) was determined as the slope derived from the linear regression of  
129  $\ln[(b_{\text{abs}})^*]$  against  $\ln(\lambda)$ , ~~is~~ over the wavelength range of 370–880 nm.

130 For the measurement of gaseous pollutants, ambient air was filtered and then drawn into a  
131 PTFE sampling line. A non-dispersive infrared analyzer (XHCO2000B) was used to measure carbon  
132 monoxide (CO), and two chemiluminescence-based analyzers (XHOZ7000 and XHN2000B) were  
133 operated to determine ozone ( $\text{O}_3$ ) and nitrogen dioxide ( $\text{NO}_2$ ), respectively. The instruments were  
134 manufactured by Hebei Sailhero Inc. (Shijiazhuang, China) in compliance with the reference  
135 methods released by the Ministry of Ecology and Environment of China.

136 The time resolutions were 1 second for PAX and 1 minute for the other instruments. Thus the  
137 raw results from PAX were converted to 1-minute averages before further analyses. The on-line  
138 measurement results were summarized in Figure 1.

## 139 2.2 Off-line measurements

140 Daytime and nighttime PM<sub>2.5</sub> samples were collected at the same site with the on-line  
141 instruments during the campaign. The sampling was done by a mass flow controlled high-volume  
142 sampler (TE-6070BLX-2.5-HVS; Tisch Environmental Inc., OH, USA), which was operated at a  
143 flow rate of 1.13 m<sup>3</sup>/min using pre-baked quartz-fiber filters (Pall Corp., NY, USA). To avoid rush  
144 hours, the daytime and nighttime samples were collected from 9:00 to 16:00 and from 21:00 to 5:00  
145 of the next day, respectively.

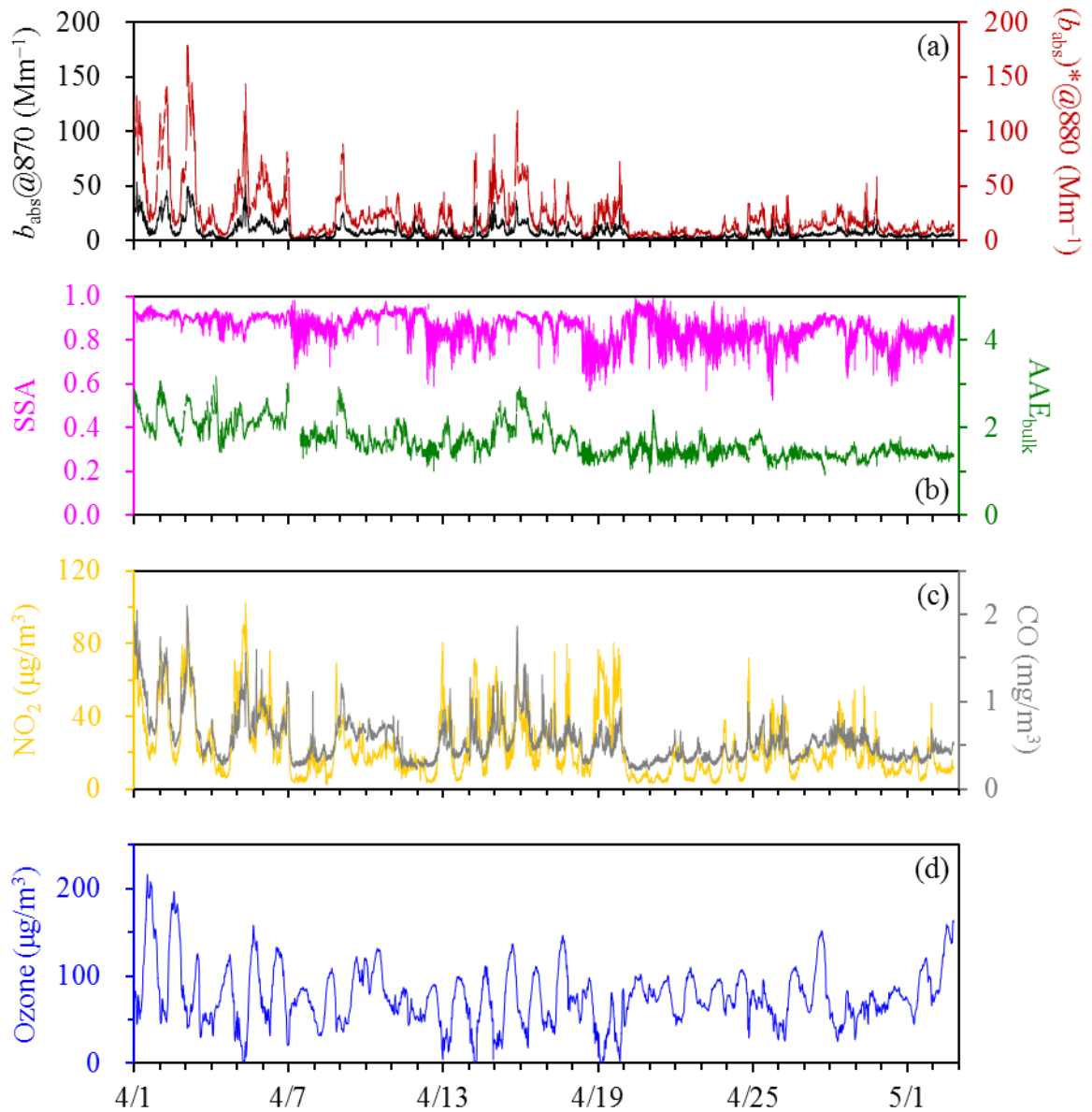
146 Organic carbon (OC) and elemental carbon (EC) of the filter samples were measured by a  
147 thermal/optical carbon analyzer (DRI-2001; Atmoslytic Inc., CA, USA), using the IMPROVE-A  
148 temperature protocol with the transmittance charring correction. The carbon analyzer also provided  
149 optical attenuation (ATN) results for the filter samples. ATN was calculated as  $\ln(I_{\text{final}}/I_{\text{initial}})$ , where  
150  $I_{\text{initial}}$  and  $I_{\text{final}}$  indicate the filter transmittance signals ( $I$ ) measured at the beginning (i.e., when the  
151 particle-laden filter has not been heated) and the end (i.e., when all the deposited carbon has been  
152 combusted off the filter) of thermal-optical analysis, respectively. Then the absorption coefficient  
153 ( $\text{Mm}^{-1}$ ) could be determined as  $\text{ATN} \times A/V$ , where  $A$  is the filter area loaded with particles ( $\text{mm}^2$ )  
154 and  $V$  is the volume of the air sampled ( $\text{m}^3$ ). It should be noted that when using the carbon analyzer,  
155 the absorption coefficients were derived at a single wavelength of 632 nm without any correction,  
156 for either the loading effect or the multiple scattering effect.

157 Water extracts of the filter samples were analyzed for inorganic ions using an ion  
158 chromatography system. The samples were also extracted by methanol to measure brown carbon  
159 (BrC). Light absorption spectra of the methanol extracts were detected over the wavelength range  
160 of 200–1110 nm, using a spectrophotometer (Ocean Optics Inc., FL, USA) coupled with a 2.5m

161 long liquid waveguide capillary cell (LWCC; World Precision Instruments Inc., FL, USA). The  
162 absorption coefficients determined in this approach, which were actually the absorption coefficients  
163 of the dissolved brown carbon (i.e., methanol-soluble BrC), will be referred to as  $(b_{\text{abs}})_{\text{MS-BrC}}$ .

### 164 **2.3 Open-access data**

165 Air quality data, e.g., hourly PM<sub>2.5</sub> and PM<sub>10</sub> concentrations, were obtained from a nearby air  
166 quality monitoring site (~2 km away from the HIT site) operated by the China National  
167 Environmental Monitoring Center (CNEMC; <https://air.cnemc.cn:18007/>). Meteorological data  
168 (e.g., temperature, relative humidity and wind speed) were obtained with a time resolution of 1  
169 hour from Weather Underground (<https://www.wunderground.com/>).



170

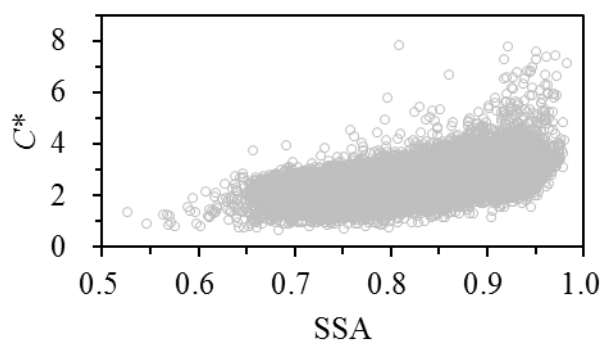
171 **Figure 1.** Time series of (a) the PAX-based  $b_{\text{abs}}$  at 870 nm and the AE33-based  $(b_{\text{abs}})^*$  at 880 nm,  
 172 (b) the PAX-based SSA and the AE33-based  $\text{AAE}_{\text{bulk}}$ , (c)  $\text{NO}_2$  and CO, and (d) ozone. The results  
 173 were shown with a time resolution of 1 minute.

### 174 3. Results and discussion

#### 175 3.1 Integrating optical parameters derived from different methods

176 We first compared the light absorption coefficients derived from the PAX at 870 nm and from  
 177 the AE33 at 880 nm, which will be termed  $b_{\text{abs}}@870$  and  $(b_{\text{abs}})^*@880$ , respectively. The  $b_{\text{abs}}@870$   
 178 results were not subject to artifacts associated with filter-based absorption measurement, as they

179 were ~~obtaining~~ obtained using *in-situ* technology. For  $(b_{\text{abs}})^*_{@880}$ , although the loading effect had  
180 been accounted for, other artifacts still existed, which could be attributed mainly to the multiple  
181 scattering by the filter fibers and the scattering by the particles embedded in the filter. The  
182 experimental setup used in this study did not allow distinguishing the two artifacts. However, their  
183 overall effect could be determined by comparing  $(b_{\text{abs}})^*_{@880}$  with  $b_{\text{abs}}_{@870}$ . The  $(b_{\text{abs}})^*_{@880}$  to  
184  $b_{\text{abs}}_{@870}$  ratios, which will be termed  $C^*$ , generally exhibited a normal distribution for the spring  
185 campaign, with a mean of 2.67 and a standard deviation of 0.54 (Figure S1). The values suggested  
186 that the overall effect of multiple scattering and aerosol scattering resulted in a significant  
187 overestimation of light absorption by  $(b_{\text{abs}})^*_{@880}$ . Further investigations indicated that the variation  
188 of  $C^*$  was closely related to SSA (Figures 2 and S2; Table 1). The median  $C^*$  was as low as 1.24 for  
189 the lower end of SSA (below 0.60) encountered in the spring campaign. Then  $C^*$  increased sharply  
190 as SSA became higher, e.g., with a median of 2.06 for the SSA range of 0.65–0.70. However, the  
191 variation of  $C^*$  was largely flattened when SSA further increased. For example, compared to that  
192 observed for the SSA range of 0.65–0.70, the median  $C^*$  was only ~0.4 higher when SSA reaching  
193 0.80–0.85. Finally, with increasing SSA, the increase of  $C^*$  became sharp again, e.g., with a median  
194  $C^*$  of 3.27 for the higher end of SSA (0.95–1.00). The clear dependence of  $C^*$  on SSA suggested the  
195 limitation of using a fixed value for the scattering-associated correction in filter-based absorption  
196 measurement. To enhance the relevance of time-resolved  $C^*$  to future studies, the median values of  
197  $C^*$  were presented in Table 1 for various SSA bins (from below 0.60 to above 0.95), which covered  
198 the typical SSA levels observed for ambient conditions. We applied the SSA-dependent median  $C^*$   
199 (Table 1) to AE33 and found that the corrected  $(b_{\text{abs}})^*_{@880}$  were in reasonable agreement with  
200  $b_{\text{abs}}_{@870}$  (Figure 3a), demonstrating the practicability of the SSA-dependent  $C^*$  results.



201

202 **Figure 2.** Dependence of  $C^*$  on SSA, both of which had a time resolution of 1 minute. Results  
 203 involved in this figure were for the entire measurement period.

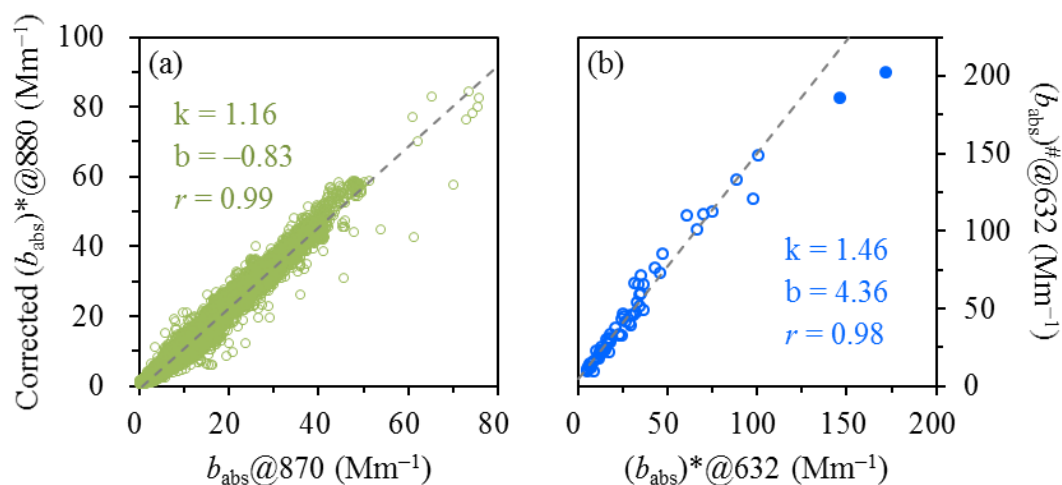
204 **Table 1.** SSA-dependent  $C^*$  results determined during the spring campaign.

SSA range	0.50– 0.60	0.60– 0.65	0.65– 0.70	0.70– 0.75	0.75– 0.80	0.80– 0.85	0.85– 0.90	0.90– 0.95	0.95– 1.00
Median $C^*$	1.24	1.65	2.06	2.24	2.26	2.46	2.76	3.06	3.27
Lower quartile of $C^*$	0.90	1.34	1.66	1.78	1.89	2.17	2.46	2.72	2.91
Upper quartile of $C^*$	1.35	2.07	2.40	2.53	2.62	2.77	3.07	3.40	3.92
Fraction in total data points (%)	0.03	0.12	1.37	4.40	11.89	24.73	30.30	26.53	0.64

205 We then compared the light absorption coefficients determined by the AE33 and off-line carbon  
 206 analyzer. The off-line results, which were obtained at 632 nm with no correction, will be specified  
 207 as  $(b_{\text{abs}})^{\#}@632$ . To align with  $(b_{\text{abs}})^{\#}@632$ , the AE33-based absorption coefficients at the same  
 208 wavelength, i.e.,  $(b_{\text{abs}})^{*}@632$ , were converted from the directly-measured  $(b_{\text{abs}})^{*}$  at 660 nm using  
 209  $AAE_{\text{bulk}}$ , which described the wavelength dependence of  $(b_{\text{abs}})^{*}$ . The time-resolved  $(b_{\text{abs}})^{*}@632$   
 210 results were first averaged for the filter sampling segments and then compared to the off-line  
 211  $(b_{\text{abs}})^{\#}@632$ . As shown in Figure 3b, the off-line measurements always resulted in higher absorption  
 212 coefficients compared to AE33, and their relationship could be approximated by the following linear  
 213 function:  $(b_{\text{abs}})^{\#}@632 = 1.46 \times (b_{\text{abs}})^{*}@632 + 4.36$  ( $r = 0.98$ ). As the differences in measurement  
 214 wavelength and time resolution had been accounted for, a likely cause for the observed

215 discrepancies was the difference in filter media used by the two instruments. As stated in the  
216 Methods section, the carbon analyzer used quartz filters, whereas the AE33 was operated with  
217 M8060 filter tapes. Although the material of M8060 was not specified by the AE33 manufacture,  
218 the multiple scattering correction factors of M8060 were determined to be generally comparable  
219 with the previously used M8020 (i.e., PTFE-coated glass-fiber filter), e.g., with relative standard  
220 deviations of within 5% for different types of sites in Europe (Yus-Díez et al., 2021). Field  
221 campaigns conducted at various locations suggested that compared to M8020, quartz filter showed  
222 stronger multiple scattering effect and thus required a higher correction factor, e.g., 2.14 vs. 1.57 for  
223 the fresh aerosols in Klagenfurt, Austria (Drinovec et al. (2015) and 3.43 vs. 2.64 for the aged  
224 aerosols in Milan, Italy (Ferrero et al., 2021). This indicated that when running two AE33 side-by-  
225 side with different filter media, quartz filter would lead to higher  $(b_{\text{abs}})^*$  than M8020, by factors of  
226 about 1.3–1.4. A comparable discrepancy was observed in St. Louis for the absorption coefficients  
227 measured by quartz and glass-fiber filters, which differed by a factor of 1.41 (Snyder and Schauer,  
228 2007). These ratios ( $\sim 1.3$ – $1.4$ ) were close to the slope shown in Figure 3b, indicating that the  
229  $(b_{\text{abs}})^{\#}@632$  vs.  $(b_{\text{abs}})^*@632$  discrepancies could be attributed primarily to the use of different types  
230 of filters in off-line and on-line measurements. In addition, it was noticed that the linear dependence  
231 of  $(b_{\text{abs}})^{\#}@632$  on  $(b_{\text{abs}})^*@632$  did not hold for the two heavily-loaded samples collected on the  
232 nights of April 1 and 2, 2023, which showed the highest carbon loadings (above  $115 \mu\text{gC}/\text{cm}^2$  for  
233 the sum of OC and EC) and ATN levels (exceeding  $\sim 2.5$ ) ~~PM<sub>2.5</sub> concentrations (exceeding 165~~  
234  ~~$\mu\text{g}/\text{m}^3$ )~~ throughout the campaign. For these two heavily-loaded samples, the ratios of  $(b_{\text{abs}})^{\#}@632$   
235 to  $(b_{\text{abs}})^*@632$  were only 1.27 and 1.18, respectively. It appeared that the absorption coefficients  
236 derived from the carbon analyzer could be biased low at high filter loadings. This artifact was to

237 some extent similar to the loading effect in the Aethalometer measurement but seemed unapparent  
 238 at relatively low filter loadings.



239

240 **Figure 3. (a)** Comparison of the corrected  $(b_{\text{abs}})^*_{@880}$  and the PAX-based  $b_{\text{abs}}@870$  for the entire  
 241 measurement period. The two parameters had the same time resolution of 1 minute and showed a  
 242 median RSD (relative standard deviation) of 8.5%. The correction of  $(b_{\text{abs}})^*_{@880}$  was based on the  
 243 median  $C^*$  values in Table 1. **(b)** Comparison of  $(b_{\text{abs}})^{\#}_{@632}$  and  $(b_{\text{abs}})^*_{@632}$ . The former was  
 244 directly derived from the carbon analyzer without any correction, while the latter was obtained by  
 245 extrapolating the AE33-based  $(b_{\text{abs}})^*_{@660}$  to 632 nm. ~~The time-resolved  $(b_{\text{abs}})^*_{@632}$  results were~~  
 246 ~~first averaged for the filter sampling segments and then compared to the off-line  $(b_{\text{abs}})^{\#}_{@632}$ .~~ In (a)  
 247 and (b), the dashed lines indicate the linear regression results with  $k$  as the slope and  $b$  as the  
 248 intercept. In (b), the linear dependence did not hold for two heavily loaded filters which were  
 249 highlighted by the solid circles.

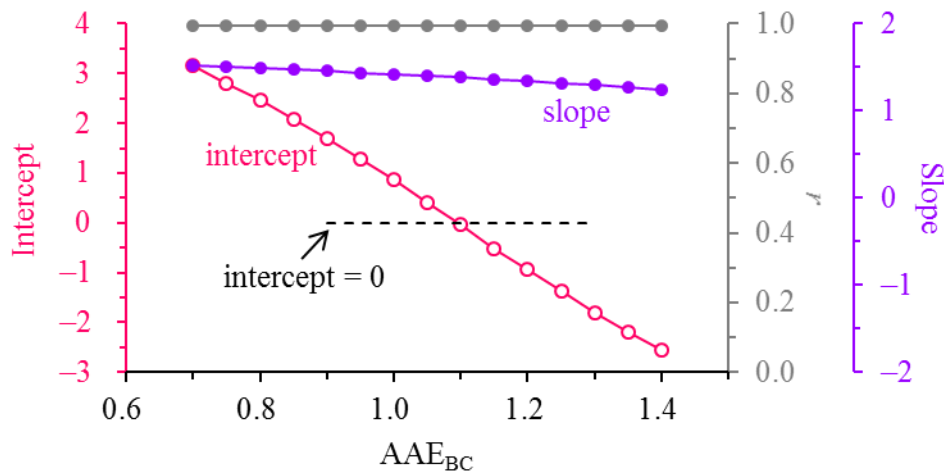
250 We also compared the brown carbon results measured by the AE33 and off-line (i.e., methanol  
 251 extraction) approaches. It has been widely accepted that methanol could dissolve the vast majority  
 252 (e.g., ~90%) of organic aerosol, making methanol-soluble OC (MSOC) a frequently-used surrogate  
 253 for BrC (Laskin et al., 2015, 2025). The absorption coefficients of MSOC, which were directly  
 254 measured, will be primarily investigated at 365 nm and the corresponding results will be termed  
 255  $(b_{\text{abs}})_{\text{MS-BrC}}@365$ . For AE33, the absorption coefficient of BrC at 370 nm was calculated as:

$$256 \quad (b_{\text{abs}})_{\text{BrC}}@370 = b_{\text{abs}}@370 - b_{\text{abs}}@880 \times (880/370)^{\text{AAE}_{\text{BrC}}} \quad (1)$$

257 In Equation (1),  $(b_{\text{abs}})@370$  and  $(b_{\text{abs}})@880$  indicate the absorption coefficients at 370 and 880 nm,

258 respectively, both of which had been corrected for the scattering-associated artifacts using the  $C^*$   
259 values in Table 1;  $AAE_{BC}$  is the absorption Ångström exponent of black carbon, a parameter  
260 describing the wavelength dependence of BC-induced light absorption. Two assumptions were  
261 involved in the calculation, including (i) the light absorption coefficient measured at 880 nm could  
262 be attributed only to black carbon and (ii) the coefficients observed at shorter wavelengths could be  
263 broken down into the contributions from BC and BrC (Lack and Langridge, 2013). A variety of  
264  $AAE_{BC}$  were tested in this study, first from 0.7 to 1.4 with an increment of 0.05. As shown in Figure  
265 4, the AE33-based  $(b_{abs})_{BrC}@370$  and the solution-based  $(b_{abs})_{MS-BrC}@365$  kept strong correlation  
266 (with  $r$  staying above 0.99) regardless of the values assumed for  $AAE_{BC}$ . In addition, when  
267 increasing the  $AAE_{BC}$  from 0.7 to 1.4, the regression slope decreased slowly from 1.52 to 1.24  
268 whereas the intercept changed sharply from +3.16 to -2.56. The intercept turned from a positive  
269 value into negative when the  $AAE_{BC}$  was changed from 1.05 to 1.10. Thus we further tested various  
270  $AAE_{BC}$  values in this range with a smaller increment of 0.01. The intercept was found to be closest  
271 to zero ( $-4.1 \times 10^{-2}$ ) for an  $AAE_{BC}$  value of 1.10 (Figure S3), e.g., compared to an intercept of  
272  $+5.2 \times 10^{-2}$  for an  $AAE_{BC}$  of 1.09. It appeared that a reasonable correlation could be reached for the  
273 on-line and off-line BrC results by assuming  $AAE_{BC} = 1.10$ . However, a slope of 1.38 retrieved  
274 under this assumption suggested that the AE33-based absorption coefficients of BrC were  
275 considerably higher than results from the methanol extracts of filter samples. This discrepancy  
276 should be associated with the states of the measured BrC, since particulate brown carbon has been  
277 found to show higher absorption coefficients than dissolved BrC (Liu et al., 2013; Washenfelder, et  
278 al., 2015). Another likely cause for this discrepancy was the OC insoluble in methanol (MIOC),  
279 which could be a considerable contributor to BrC absorption but was missed by the solution-based

280 approach for BrC determination (Atwi et al., 2022).



281

282 **Figure 4.** Slope, intercept and  $r$  determined by regressing the AE33-based  $(b_{\text{abs}})_{\text{BrC}@370}$  against the  
283 solution-based  $(b_{\text{abs}})_{\text{MS-BrC}@365}$ . Different  $\text{AAE}_{\text{BrC}}$  values were assumed to retrieve the time-  
284 resolved  $(b_{\text{abs}})_{\text{BrC}@370}$ , which were first averaged for the filter sampling segments and then used  
285 for the regression.

### 286 3.2 Identification of different episodes

287 There have been numerous evidences suggesting pronounced influences of aerosol sources on  
288 the mass absorption efficiency of brown carbon ( $\text{MAE}_{\text{BrC}}$ ), which is defined as the ratio of BrC's  
289 absorption coefficient to its mass concentration. For example, regarding seasonal variations,  
290  $\text{MAE}_{\text{BrC}}$  typically peaked in winter due to increased emissions from coal combustion and/or biomass  
291 burning (Mo et al., 2024). In addition,  $\text{MAE}_{\text{BrC}}$  were found to show diurnal variations with higher  
292 nighttime levels during winter in Northeast China, and this pattern was inferred to be driven  
293 primarily by the emissions from heavy-duty diesel trucks, which were allowed to operate only at  
294 night for the main urban area (Cheng et al., 2023). Spatial variations were also evident for  $\text{MAE}_{\text{BrC}}$ ,  
295 e.g., water-soluble BrC, which was strongly associated with SOA, was observed to be more  
296 absorbing in Los Angeles compared to Atlanta (Zhang et al., 2011). In that study, SOA were traced  
297 back mainly to anthropogenic VOCs for Los Angeles, and to biogenic precursors for Atlanta. The

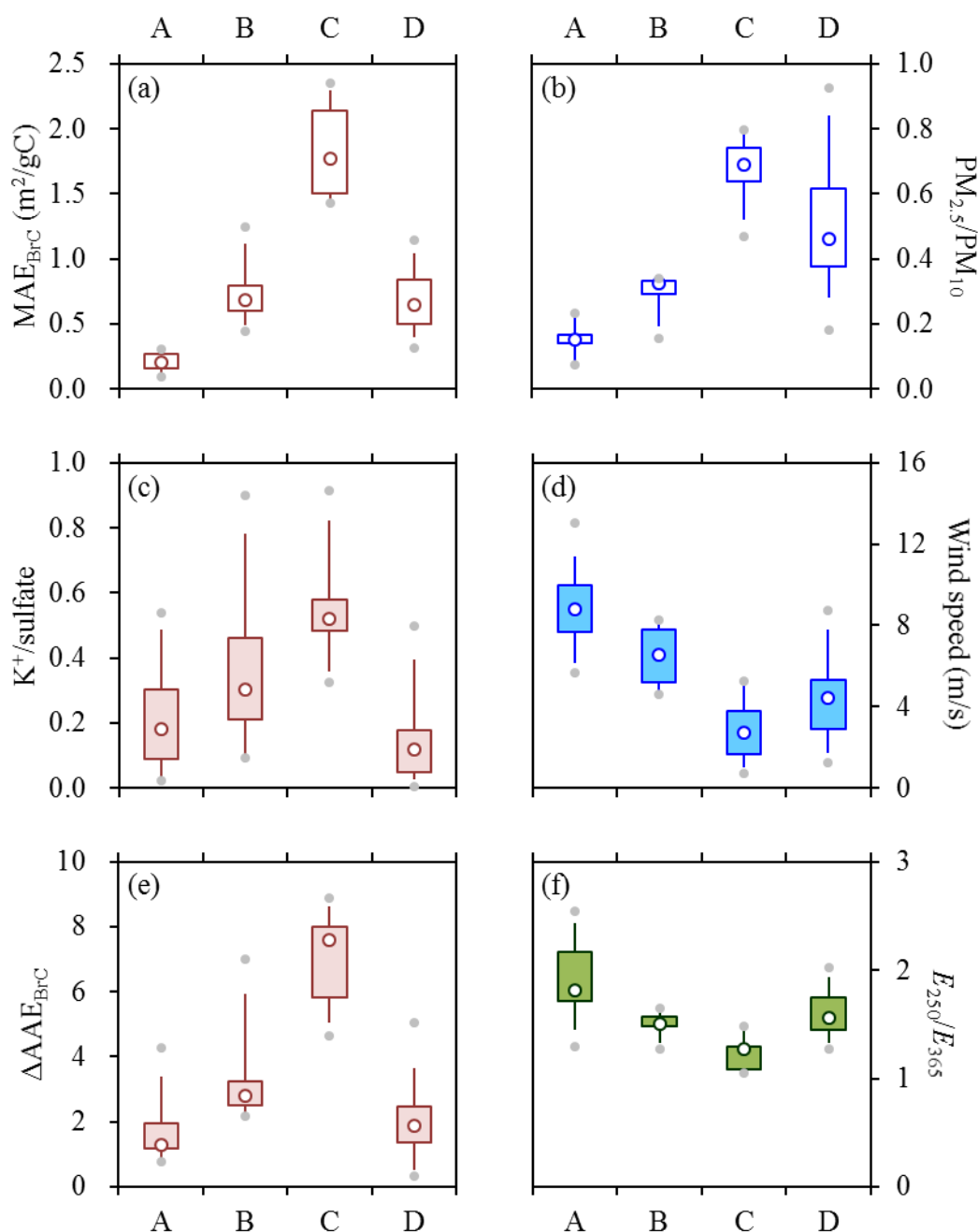
298 authors then speculated that secondary BrC from anthropogenic precursors likely had stronger  
299 capacities of light absorption compared to biogenic SOA, while this inference was confirmed shortly  
300 by chamber studies (Lambe et al., 2013; Liu et al., 2016).

301       Given its close association with aerosol sources, in this study, MAE<sub>BrC</sub> was first investigated  
302 to distinguish different types of pollution episodes. To avoid the omission of MIOC contribution,  
303 we applied the bulk BrC light absorption from AE33 and calculated MAE<sub>BrC</sub> as the ratio of  
304  $(b_{\text{abs}})_{\text{BrC}@370}$  to OC. For each filter sample, the off-line OC was used as BrC mass while the  
305 corresponding BrC absorption coefficient took the average of the AE33-based results during the  
306 filter sampling period. The MAE<sub>BrC</sub> results were found to vary significantly (from 0.12 to 3.23  
307 m<sup>2</sup>/gC) during the spring campaign, pointing to changeable drivers for the haze pollution. Two  
308 groups of samples were most noticeable, showing MAE<sub>BrC</sub> levels at the lower and higher ends of  
309 the spring results, respectively. The first group ( $N = 13$ , case A in Figure 5) had a MAE<sub>BrC</sub> range of  
310 0.12 to 0.40 m<sup>2</sup>/gC (Figure 5a), and the samples exhibited the following characteristics (Figures 5b–  
311 5d): relatively low ratios of PM<sub>2.5</sub> to PM<sub>10</sub> (0.15 in terms of median value; same hereafter), relatively  
312 high wind speeds (8.77 m/s), and relatively low ratios of K<sup>+</sup> to sulfate (0.18). The PM<sub>2.5</sub> to PM<sub>10</sub>  
313 ratio (PM<sub>2.5</sub>/PM<sub>10</sub>) was strongly related to the dust influence, typically with a decreasing trend as  
314 the dust impact became stronger (Putaud et al., 2010). Thus for the first group of samples, the  
315 reduced PM<sub>2.5</sub>/PM<sub>10</sub> together with the elevated wind speeds presumably indicated considerable  
316 influences of dusts. In addition, observational results from Northeast China suggested that  
317 agricultural fires could effectively enhance the abundances of K<sup>+</sup> but was not a significant  
318 contributor to sulfate (Cheng et al., 2021), resulting in spikes of K<sup>+</sup> to sulfate ratios (K<sup>+</sup>/sulfate) that  
319 typically coincided with the peaks of levoglucosan to OC ratios (LG/OC). Thus similar to increased

320 LG/OC, enhanced  $K^+$ /sulfate could also be used as an indicator for agricultural fires. Conversely,  
321 reduced  $K^+$ /sulfate could be translated into little impact of open burning. The clear association  
322 between  $K^+$ /sulfate and agricultural fires was also supported by the contrasting fire hotspot detection  
323 results between periods with different  $K^+$ /sulfate levels (Figure S4). Then based on a synthesis of  
324  $PM_{2.5}/PM_{10}$ , wind speed and  $K^+$ /sulfate, it was concluded that the first group of samples were subject  
325 to strong influences of dusts but insignificant impacts from agricultural fires. Contrasting to the first  
326 group, the second group of samples ( $N = 8$ , case C in Figure 5) accompanied with the higher-end  
327  $MAE_{BrC}$  values (1.75–3.23  $m^2/gC$ ) showed quite different features (Figures 5a–5d), including higher  
328  $PM_{2.5}/PM_{10}$  (0.69), lower wind speeds (2.71 m/s) and larger  $K^+$ /sulfate (0.52). These signatures  
329 suggested strong influences of agricultural fires but little impact of dusts. In the following  
330 discussions, the first and second groups of samples will be referred to as dust-impacted and fire-  
331 impacted ones, respectively.

332 After excluding the two distinct groups discussed above, the remaining samples showed  
333 moderate  $MAE_{BrC}$  levels but considerable variations in other signatures. Some of the samples ( $N =$   
334 7, the third group; case B in Figure 5) were heavily polluted in  $PM_{10}$  ( $\sim 140\text{--}305 \mu g/m^3$ ) and  
335 exhibited mixed features of the dust-impacted and fire-impacted samples (Figures 5b–5d), with the  
336 median values of all the three signatures (i.e.,  $PM_{2.5}/PM_{10}$ , wind speed and  $K^+$ /sulfate) falling in-  
337 between the first two groups. The other samples ( $N = 35$ , the fourth group; case D in Figure 5) had  
338 substantially lower  $PM_{10}$  (averaging  $53.45 \pm 29.78 \mu g/m^3$ ) and were characterized by pretty low  
339  $K^+$ /sulfate (0.12), and moderate levels of both  $PM_{2.5}/PM_{10}$  (0.46) and wind speeds (4.44 m/s). It  
340 appeared that neither agricultural fires nor dusts exerted a strong influence on these samples, which  
341 could thus be used to represent the typical conditions of the spring campaign. In the following

342 discussions, the third and fourth groups of samples will be termed fire&dust-impacted and typical  
 343 ones, respectively. For different group of samples (i.e., cases A–D), the distributions of their  
 344 sampling segments were highly irregular during the spring campaign (Figure S5), suggesting  
 345 dramatic variations of aerosol sources for the measurement period.



346

347 **Figure 5.** Variations of (a) MAE<sub>BrC</sub>, (b) PM<sub>2.5</sub>/PM<sub>10</sub>, (c) K<sup>+</sup>/sulfate, (d) wind speeds, (e) ΔAAE<sub>BrC</sub>  
 348 and (f) E<sub>250</sub>/E<sub>365</sub> across cases of A–D, which correspond to the dust-impacted, fire&dust-impacted,  
 349 fire-impacted and typical samples, respectively. Lower and upper box bounds indicate the 25<sup>th</sup> and  
 350 75<sup>th</sup> percentiles, the whiskers below and above the box indicate the 5<sup>th</sup> and 95<sup>th</sup> percentiles, the solid

351 circles below and above the box indicate the minimum and maximum, and the open circle within  
352 the box marks the median.

353 The identification of the four groups was also supported by the spectral measurement results  
354 from the methanol extracts of filter samples. It has been commonly recognized that light absorption  
355 by brown carbon exhibits stronger wavelength ( $\lambda$ ) dependence compared to black carbon, leading  
356 to larger absorption Ångström exponent of BrC ( $AAE_{BrC}$ ). Using the solution-based light absorption  
357 spectra,  $AAE_{BrC}$  could be determined as the slope derived from the linear regression of  $\ln[(b_{abs})_{MS-BrC}]$   
358 against  $\ln(\lambda)$ . As shown by our previous study in Northeast China, when the agricultural fire  
359 impact was insignificant,  $\ln[(b_{abs})_{MS-BrC}]$  exhibited a strong linear correlation with  $\ln(\lambda)$  and thus  
360  $AAE_{BrC}$  could be readily determined over a relatively wide wavelength range of 310–460 nm  
361 (Cheng et al., 2023). During agricultural fire episodes, however, the dependence of  $\ln[(b_{abs})_{MS-BrC}]$   
362 on  $\ln(\lambda)$  tended to be non-linear, since the fire-emitted chromophores could result in a distinct  
363 absorption peak at  $\sim 365$  nm (Cheng et al., 2023). The non-linear correlation between  $\ln[(b_{abs})_{MS-BrC}]$   
364 and  $\ln(\lambda)$  was also evident for the fire-impacted samples in this study. To quantitatively describe the  
365 non-linearity, we calculated the difference in  $AAE_{BrC}$  over two wavelength ranges (i.e., 410–460  
366 and 310–360 nm) and defined this difference as  $\Delta AAE_{BrC}$  (Figure S6). As shown in Figure 5e,  
367 different groups of samples indeed showed considerable discrepancies in  $\Delta AAE_{BrC}$ . For example,  
368 the  $\Delta AAE_{BrC}$  levels were found to be highest for the fire-impacted samples (7.60 in terms of median  
369 value), moderate for the fire&dust-impacted samples (2.81), and lowest for the dust-impacted  
370 samples (1.30). In addition,  $\Delta AAE_{BrC}$  differed significantly between the fire&dust-impacted and  
371 typical samples (2.81 vs. 1.86), demonstrating the necessity for further distinguishing the two groups  
372 of samples despite their comparable  $MAE_{BrC}$  levels.

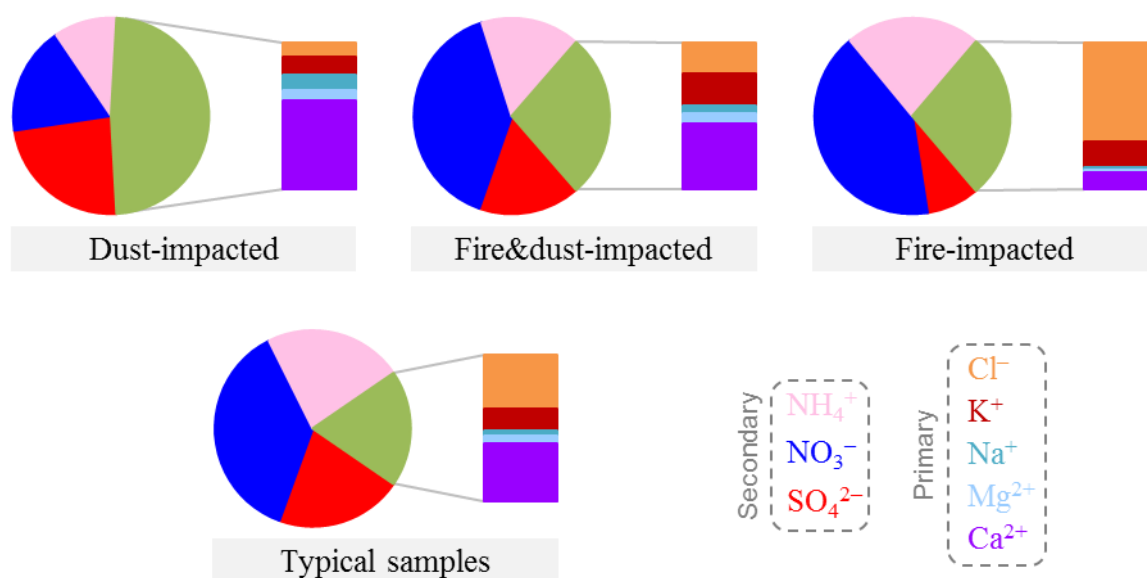
373 Another diagnostic parameter that could be derived from the light absorption spectra of MSOC

374 was the ratio of  $(b_{\text{abs}})_{\text{MS-BrC}}$  at 250 nm to that at 365 nm, which was usually termed  $E_{250}/E_{365}$ . This  
375 ratio was proposed as an indicator for the chemical properties of the dissolved organics, e.g., higher  
376  $E_{250}/E_{365}$  typically indicated smaller molecular sizes and lower aromaticity (Duarte et al., 2005;  
377 Chen et al., 2019). In this study,  $E_{250}/E_{365}$  exhibited a clear decreasing trend across the dust-impacted,  
378 fire&dust-impacted and fire-impacted samples (Figure 5f), i.e., with increasing impacts of  
379 agricultural fires. On one hand, this trend confirmed the heterogeneity of different groups of samples,  
380 from the perspective of the chemical properties of MSOC. On the other hand, this trend suggested  
381 that compared to those associated with dusts, the fire-emitted organic compounds were likely  
382 characterized by higher molecular weights and higher aromatic contents, which should be highly  
383 responsible for the strong light absorption capacities of the fire-impacted samples.

### 384 **3.3 Comparison of inorganic species across different episodes**

385 Figure 6 compares the compositions of water-soluble inorganic ions among different groups of  
386 samples. The ions were broadly separated into secondary species (i.e., sulfate, nitrate and  
387 ammonium) and primary components (i.e.,  $\text{Cl}^-$ ,  $\text{K}^+$ ,  $\text{Na}^+$ ,  $\text{Mg}^{2+}$  and  $\text{Ca}^{2+}$ ). Based on the ion  
388 concentrations averaged for each group, the dust-impacted samples were found to differ  
389 significantly from the other ones in three aspects, including higher fraction of primary species in  
390 total ions (48% vs. < 30%), larger contribution of  $\text{Ca}^{2+}$  to primary ions (61% vs. < 45%) and higher  
391 ratio of sulfate to nitrate (1.31 vs. < 0.6). The fire-impacted samples also exhibited several distinct  
392 features, including the dominant contribution of  $\text{Cl}^-$  to primary ions (68% vs. < 40% for the other  
393 groups) and the remarkably high ratio of nitrate to sulfate (4.73). Actually, the fraction of  $\text{Ca}^{2+}$  in  
394 primary ions showed a clear decreasing trend across the dust-impacted, fire&dust-impacted and fire-  
395 impacted episodes (from 61% to 12%), while an opposite trend was observed for the fraction of  $\text{Cl}^-$

396 (from 10% to 68%). These patterns were not surprising, since  $\text{Ca}^{2+}$  and  $\text{Cl}^-$  had been commonly  
 397 identified in dust and agricultural fire emissions, respectively (Bi et al., 2019). One may argue that  
 398  $\text{Cl}^-$  should be used in Section 3.2 for the separation of samples into different groups. Besides open  
 399 burning, however, there existed other important sources for  $\text{Cl}^-$  (Bi et al., 2019), e.g., coal  
 400 combustion. Given the relatively low temperatures during the spring campaign (averaging 8.5 °C  
 401 and around 0 °C for ~25% of the samples), coal combustion was expected to contribute considerably.  
 402 The prevalence of coal combustion emissions was in line with the largely comparable  $\text{Cl}^-$  to sulfate  
 403 ratios observed for the samples after excluding the fire-impacted ones (Figure S7). The substantial  
 404 contribution of  $\text{Cl}^-$  to primary ions (37%) determined for the typical samples also confirmed the  
 405 substantial contribution of coal combustion. The discussions above indicated that the relative  
 406 abundances of  $\text{Cl}^-$  could be used to isolate the periods with strong influences of fires, but were less  
 407 capable of identifying other episodes (e.g., the fire&dust-impacted samples).

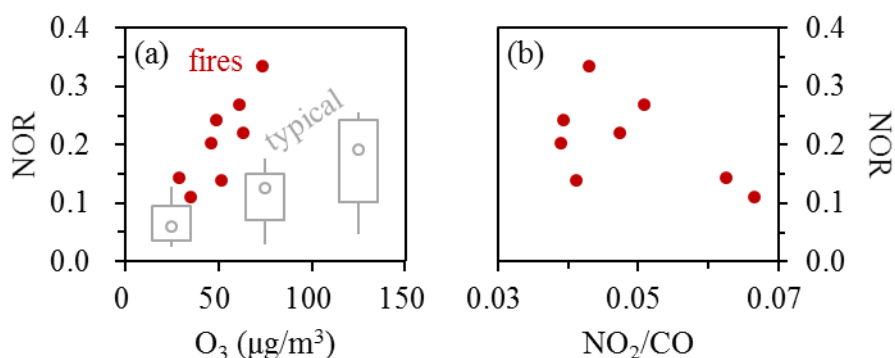


408  
 409 **Figure 6.** Comparison of water-soluble ion compositions across the dust-impacted, fire&dust-  
 410 impacted, fire-impacted and typical samples. In each pie chart, the unlabeled fraction indicates the  
 411 sum of the primary ions.

412 The fire-impacted samples showed significantly higher relative abundance of nitrate compared

413 to sulfate (Figure 6), likely pointing to enhanced formation of nitrate under strong influences of  
414 agricultural fire emissions. This inference was supported by the comparison of nitrogen oxidation  
415 ratios (NOR) among different episodes (Figure 7a). For the typical conditions of spring (i.e., as  
416 reflected by the typical samples), NOR generally exhibited an increasing trend as ozone became  
417 higher (Figure 7a), showing larger values (accompanied with elevated ozone) during the daytime  
418 (Figure S8). The positive dependence of NOR on ozone held as well for the fire-impacted samples,  
419 all of which occurred at night. However, it is noteworthy that the fire-impacted samples generally  
420 showed higher NOR values than the typical ones with comparable ozone levels. Although drivers  
421 for the increased NOR remained unclear based on the available observations, it was hypothesized  
422 that some distinct dark-reactions occurred in the agricultural fire plumes and ultimately enhanced  
423 the nitrate formation. As suggested by results from the laboratory-generated biomass burning smoke  
424 (Ahern et al., 2018) and ambient open-burning plume (Decker et al., 2019), such nocturnal processes  
425 may include the production of  $\text{NO}_3$  radicals and  $\text{N}_2\text{O}_5$ , the heterogeneous transformation of  $\text{N}_2\text{O}_5$   
426 into nitrate (e.g., on the surface of the abundant biomass-burning particles), and the reaction of  $\text{NO}_3$   
427 radicals with biomass burning VOCs (which could result in complex products including nitrate). In  
428 addition, for the fire-impacted samples, the conditions with relatively low ratios of  $\text{NO}_2$  to CO  
429 ( $\text{NO}_2/\text{CO}$ ) seemed more favorable for the enhancement of NOR (Figure 7b). Results from the  
430 laboratory measurement and satellite-based observation of biomass burning smoke suggested that  
431 decreased  $\text{NO}_2/\text{CO}$  ratios were typically associated with more smoldering combustion, which would  
432 emit large amounts of CO but was less favorable for  $\text{NO}_2$  production (van der Velde et al., 2021;  
433 Anderson et al., 2023). Thus the association between elevated NOR and reduced  $\text{NO}_2/\text{CO}$  likely  
434 indicated that the low-efficiency fires were more favorable for the nocturnal nitrate formation. It

435 should also be noted that NOR exhibited considerable sample-by-sample variations at similarly low  
 436 levels of  $\text{NO}_2/\text{CO}$  (e.g., below  $\sim 0.05$ ). A possible explanation was that the  $\text{NO}_2/\text{CO}$  values presented  
 437 in Figure 7b were the averages of the time-resolved results measured during the fire episodes, and  
 438 thus were only rough indicators for the overall burning conditions. Another likely cause was that  
 439 besides the combustion efficiency, there existed other influencing factors for NOR in the fire plumes.  
 440 The detailed chemical mechanisms for the fire-induced enhancement in nocturnal NOR, including  
 441 the roles of combustion efficiencies (which are expected to influence the profiles of the fire  
 442 emissions), merit further investigations.



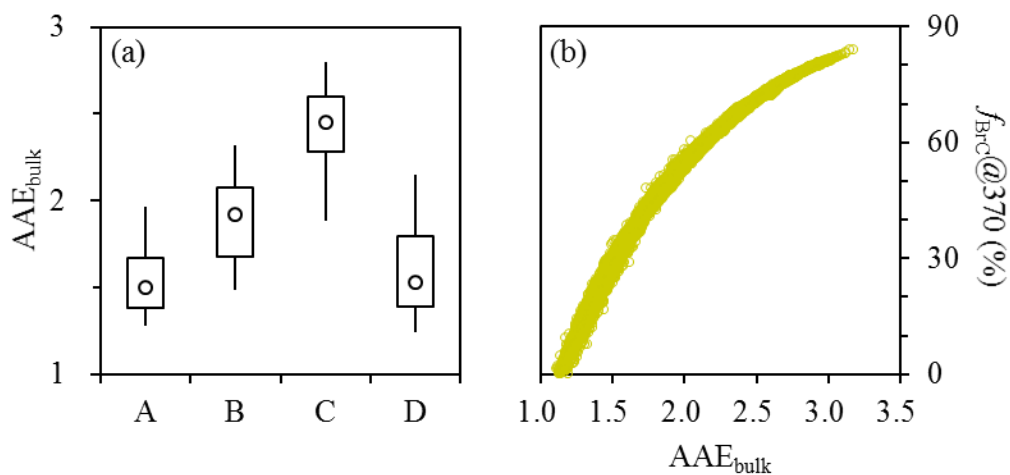
443

444 **Figure 7.** Dependences of NOR on (a) ozone (as shown by the solid circles) and (b)  $\text{NO}_2/\text{CO}$  for  
 445 the fire-impacted samples. In (a), results from the typical samples are also presented for comparison,  
 446 as shown by the overlaying box plot. Here the typical samples were divided into three subgroups  
 447 with ozone concentrations of below 50, 50–100 and 100–150  $\mu\text{g}/\text{m}^3$ , respectively. NOR was  
 448 calculated as  $n\text{-nitrate}/(n\text{-nitrate} + n\text{-NO}_2)$ , where “n” indicates the molar concentration. To align  
 449 with the off-line nitrate, the time-resolved  $\text{NO}_2$  were first averaged for the filter sampling segments  
 450 and then used for the NOR calculation.

### 451 3.4 Impacts of open burning and secondary formation on the BrC-related signatures

452 As discussed in Section 3.2, agricultural fire emissions exhibited pronounced influences on  
 453  $\text{MAE}_{\text{BrC}}$ ,  $\Delta\text{AAE}_{\text{BrC}}$  and  $E_{250}/E_{365}$ , by enhancing the light absorption capacity of bulk BrC, emitting  
 454 distinct chromophores with a characteristic absorption peak at  $\sim 365$  nm, and producing organic  
 455 compounds with relatively high molecular weights and aromatic contents, respectively. Besides

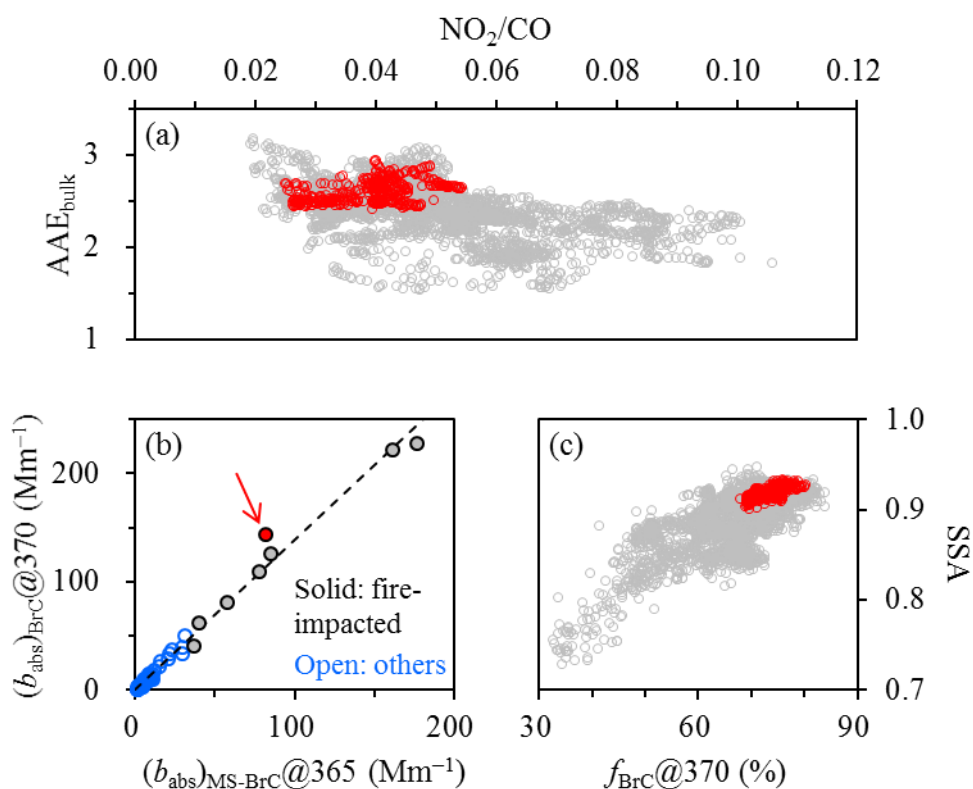
456 these signatures, the wavelength dependence of aerosol absorption ( $AAE_{\text{bulk}}$ ) and the relative  
457 importance of BrC absorption (primarily investigated at 370 nm as  $f_{\text{BrC}@370}$ ) were also  
458 significantly impacted by the fire emissions. Here  $f_{\text{BrC}@370}$  was calculated as the ratio of  
459  $(b_{\text{abs}})_{\text{BrC}@370}$  to  $(b_{\text{abs}})_{@370}$ , with  $(b_{\text{abs}})_{@370}$  obtained by applying the  $C^*$  values in Table 1 to the  
460 AE33 results and  $(b_{\text{abs}})_{\text{BrC}@370}$  determined by Equation (1) using an  $AAE_{\text{BC}}$  of 1.10 and  $(b_{\text{abs}})_{@370}$   
461 obtained by applying the  $C^*$  values in Table 1 to the AE33 results. As can be seen from Figures 8a  
462 and S9, both  $AAE_{\text{bulk}}$  and  $f_{\text{BrC}@370}$  showed clear increasing trends as the fire impacts became  
463 stronger. For example, the median  $AAE_{\text{bulk}}$  increased substantially across the dust-impacted,  
464 fire&dust-impacted and fire-impacted samples (from 1.50 to 2.45). Meanwhile, the median  
465  $f_{\text{BrC}@370}$  was enhanced by 2.5 folds, from 28% to 70%. These patterns were not surprising, given  
466 the significance of biomass burning as a BrC source (Washenfelder et al., 2015) and the fact that the  
467 light absorption by BrC typically shows stronger wavelength dependence, i.e., increases more  
468 sharply towards shorter wavelengths, compared to BC. In addition, it appeared that  $AAE_{\text{bulk}}$  could  
469 be used considered as an alternative estimate for the BrC contribution to aerosol absorption, since a  
470 consistent dependence of  $f_{\text{BrC}@370}$  on  $AAE_{\text{bulk}}$  was observed for different episodes, regardless of  
471 the variations of aerosol sources (Figure 8b).



472

473 **Figure 8. (a)** Variation of  $AAE_{\text{bulk}}$  across cases of A–D, which correspond to the dust-impacted,  
474 fire&dust-impacted, fire-impacted and typical samples, respectively. **(b)** Relationship between  
475  $f_{\text{BrC}@370}$  and  $AAE_{\text{bulk}}$  (results from different cases were not distinguished). Time-resolved  $AAE_{\text{bulk}}$   
476 and  $f_{\text{BrC}@370}$  were first extracted for the filter sampling segments and then used for the comparisons.

477 For the agricultural fire episodes,  $AAE_{\text{bulk}}$  generally exhibited a negative dependence on the  
478 ratio of  $\text{NO}_2$  to  $\text{CO}$  ( $\text{NO}_2/\text{CO}$ ), e.g., elevated  $AAE_{\text{bulk}}$  usually occurred at relatively low  $\text{NO}_2/\text{CO}$   
479 levels (Figure 9a). Recalling the association between decreased  $\text{NO}_2/\text{CO}$  and more smoldering  
480 combustion, the low-efficiency fire emissions were presumably an important driver for the increase  
481 of  $AAE_{\text{bulk}}$ , i.e., the enhancement of  $f_{\text{BrC}@370}$ . In addition, one fire-impacted sample (collected on  
482 the night of April 15, 2023) was noticed to exhibit relatively large discrepancy between the AE33-  
483 based  $(b_{\text{abs}})_{\text{BrC}@370}$  and the solution-based  $(b_{\text{abs}})_{\text{MS-BrC}@365}$  (Figure 9b), likely suggesting an  
484 increase in the fraction of methanol-insoluble species in total OC. This sample was also  
485 characterized by relatively low levels of  $\text{NO}_2/\text{CO}$ , pointing to the prevalence of low-efficiency fires  
486 for the sampling period and the potential contribution of such fires to methanol-insoluble OC. This  
487 inference was partially supported by association of reduced  $E_{250}/E_{365}$  with decreased  $\text{NO}_2/\text{CO}$   
488 (Figure S10), which indicated that the low-efficiency fires favored the emissions of organic  
489 compounds with relatively high molecular weights and aromatic contents. It is also noteworthy that  
490 although the BrC particles from agricultural fires, especially those with low efficiencies, contributed  
491 considerably to aerosol absorption in the ultraviolet wavelength range, they likely appeared more  
492 scattering at 870 nm, the wavelength for the PAX-based SSA determination. For example, SSA  
493 exhibited a clear increasing trend as  $f_{\text{BrC}@370}$  became higher (Figure 9c), indicating that the BrC  
494 particles exerted limited impact on the aerosol absorption at 870 nm.

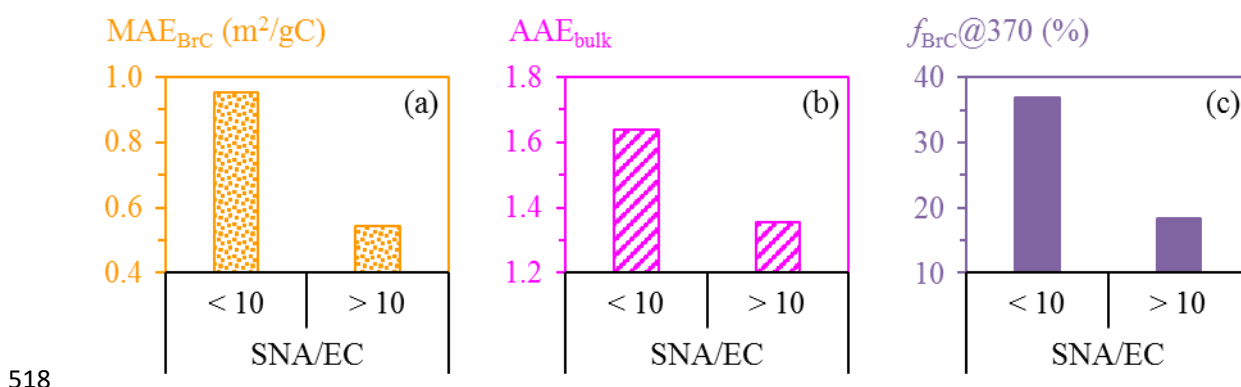


495

496 **Figure 9.** (a) Relationship between time-resolved  $AAE_{\text{bulk}}$  and  $NO_2/CO$  for the fire episodes. (b)  
 497 Comparison of the AE33-based  $(b_{\text{abs}})_{\text{BrC}@370}$  and the filter-based  $(b_{\text{abs}})_{\text{MS-BrC}@365}$ . (c)  
 498 Relationship between time-resolved SSA and  $f_{\text{BrC}@370}$  for the fire episodes. In (b), results from the  
 499 fire-impacted and other samples were shown separately, while the dashed line indicates the linear  
 500 regression result determined based on all of the spring samples. The sample collected on the night  
 501 of April 15, 2023 was indicated by the arrow. In (a) and (c), results during the collection period of  
 502 this specific sample were also highlighted, as shown by the red data points.

503 SOA formation was identified as another influencing factor for BrC. Here we focused on the  
 504 typical samples to minimize the impacts of agricultural fires and dusts. Although SOA tracer was  
 505 not directly measured in this study, the ratio of SNA (i.e., the sum of secondary inorganic ions  
 506 including sulfate, nitrate and ammonium) to EC could be used as an indirect indicator for the  
 507 significance of SOA formation. The effectiveness of this indicator was supported by the concurrent  
 508 enhancements in SNA and SOA repeatedly observed in Harbin (Cheng et al., 2021; Cheng and He,  
 509 2026). As shown in Figure 10a,  $MAE_{\text{BrC}}$  dropped considerably once the SNA to EC ratio (SNA/EC)  
 510 exceeded 10, with the median  $MAE_{\text{BrC}}$  almost halved (from 0.95 to 0.51  $m^2/gC$ ). It appeared that

511 the bulk BrC tended to be less absorbing as more SOA was produced. This pattern was with  
 512 expectation, since SOA typically had weaker light absorption capacities than primary organic  
 513 matters (Kumar et al., 2018; Cappa et al., 2020). Similar to  $MAE_{BrC}$ ,  $AAE_{bulk}$  and  $f_{BrC}@370$  were  
 514 also substantially lower for the SNA/EC range of above 10 (Figures 10b–c), with their median  
 515 values decreasing from 1.64 to 1.35 and from 37% to 18%, respectively. The discussions above  
 516 suggested that SOA formation could reduce the MAE of bulk BrC and the influence of BrC on the  
 517 total light absorption of aerosol.



518  
 519 **Figure 10.** Comparisons of (a)  $MAE_{BrC}$ , (b)  $AAE_{bulk}$  and (c)  $f_{BrC}@370$  with SNA/EC ratios of below  
 520 and above 10, for the typical samples. Time-resolved  $AAE_{bulk}$  and  $f_{BrC}@370$  were first extracted for  
 521 the filter sampling segments and then used for the comparisons. Only the median values are shown  
 522 here. Refer to Figure S11 for detailed comparisons.

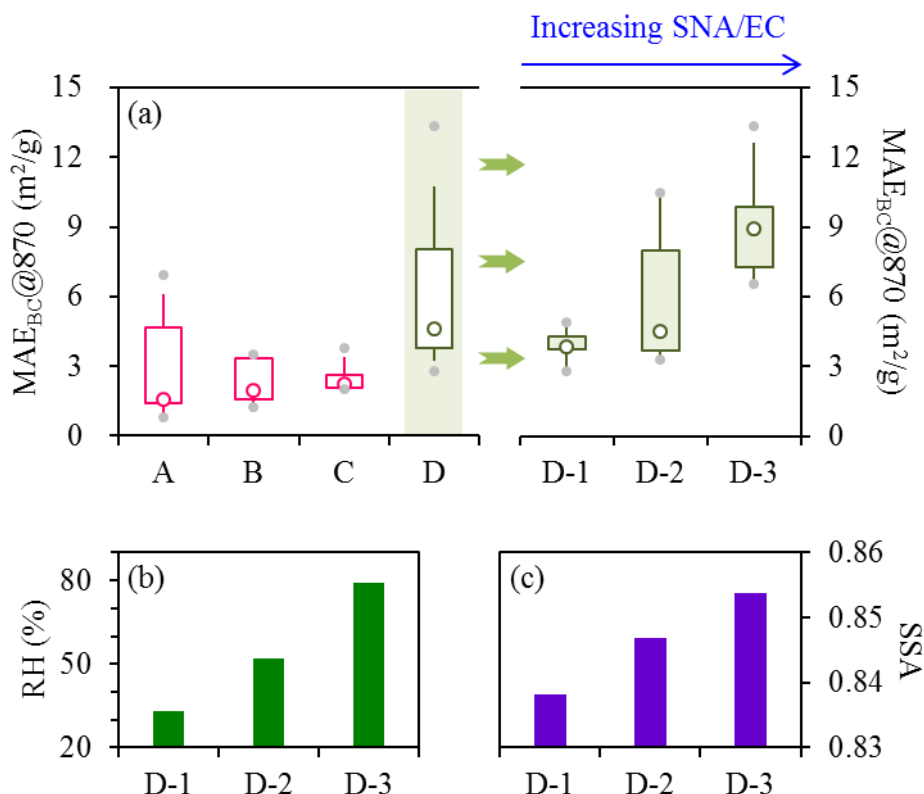
### 523 3.5 Evidences for considerable light absorption enhancement of black carbon

524 Similar to  $MAE_{BrC}$ , the mass absorption efficiency of BC ( $MAE_{BC}$ ) was calculated as the ratio  
 525 of the PAX-based ( $b_{abs}$ )@870 to EC, and the results were specified as  $MAE_{BC}@870$ . A consensus  
 526 had been reached that the mass absorption efficiency of uncoated black carbon should be at least 5  
 527  $m^2/g$  at 550 nm (Bond et al., 2013; Petzold et al., 2013). This lower limit, which was suggested as a  
 528 fundamental physical property of black carbon, could be converted to a threshold value of 3.02  $m^2/g$   
 529 at 870 nm (using an  $AAE_{BC}$  of 1.1). For the dust-impacted, fire&dust-impacted and fire-impacted

530 episodes, the majority (~55–90%) of the samples showed  $MAE_{BC@870}$  values smaller than 3.02  
531  $m^2/g$ , and the median  $MAE_{BC@870}$  were only 1.59, 1.95 and 2.25  $m^2/g$ , respectively (Figure 11a).  
532 Such unrealistically low  $MAE_{BC@870}$  could hardly be explained by uncertainties in the PAX-based  
533 absorption measurement but pointed to overestimation of black carbon mass by EC. In thermal-  
534 optical analysis, the interfering components for EC determination may include carbonate and brown  
535 carbon, which were closely associated with dusts and biomass burning, respectively. For example,  
536 previous studies suggested that calcium carbonate ( $CaCO_3$ ) did not completely decompose at 650 °C  
537 when heated in an inert atmosphere (Karanasiou et al., 2011), and tar balls from open burning could  
538 retain ~30% of their volumes at 600 °C (Adachi et al., 2017; Sedlacek III et al., 2018). For the  
539 IMPROVE-A temperature protocol used in this study, the peak temperature of the inert mode was  
540 580 °C. Thus when the dust and/or agricultural fire impacts were significant, it was very likely that  
541 a fraction of the carbonate and/or brown carbon could slip into the oxidizing mode of the analysis  
542 and then be misidentified as EC. It is also noteworthy that among the fire episodes, the events with  
543 unrealistically low  $MAE_{BC@870}$  values (e.g., around 2  $m^2/g$ ) typically showed relatively smaller  
544  $NO_2/CO$  (Figure S12), suggesting the low-efficiency fires as an important source for the interfering  
545 species in thermal-optical EC measurement.

546 The overestimation of EC mass became non-evident for the typical samples, as indicated by  
547 their  $MAE_{BC@870}$  levels which stayed above ~3  $m^2/g$  (Figure 11a). In addition, the  $MAE_{BC@870}$   
548 values were found to exhibit significant sample-by-sample variations. In general,  $MAE_{BC}$  is strongly  
549 influenced by the particle mixing state, with relatively low levels for uncoated black carbon. As BC  
550 is internally mixed with (i.e., coated by) non-refractory components (e.g., sulfate),  $MAE_{BC}$  typically  
551 tends to increase to varying degrees, and the specific magnitude depends on many factors such as

552 the complex refractive index of the coating materials (Liu et al., 2014) and the detailed particle  
553 morphology (e.g., the position of BC within the coating materials; Huang et al., 2024). In this study,  
554 the variations of  $MAE_{BC@870}$  were closely related to the changes in SNA/EC. As shown in Figure  
555 11a,  $MAE_{BC@870}$  showed a clear increasing trend across the SNA/EC ranges of below 5, 5–10 and  
556 above 10, with the median  $MAE_{BC@870}$  increasing from 3.83 to 4.53  $m^2/g$  and finally reaching  
557 8.94  $m^2/g$ . SNA/EC was not only a direct measure of secondary inorganic aerosol production but  
558 also an indirect indicator for SOA formation (as discussed in Section 3.4). Thus the positive  
559 dependence of  $MAE_{BC@870}$  on SNA/EC was presumably driven by secondary aerosols, which  
560 could effectively enhance BC absorption by internal mixing. Using the median  $MAE_{BC@870}$   
561 determined for the SNA/EC range of below 5 as the reference, the light absorption enhancement  
562 ( $E_{abs}$ ) factors were estimated to be 1.18 and 2.33 for the SNA/EC ranges of 5–10 and above 10,  
563 respectively. Given that RH increased substantially across the three SNA/EC ranges (Figure 11b),  
564 heterogeneous reactions involving aerosol water was inferred to be highly favorable for the  
565 secondary aerosol production and BC absorption enhancement. In addition, SSA elevated slightly  
566 with increasing SNA/EC (Figure 11c), indicating that the particles tended to be more scattering as  
567 the secondary aerosol formation was enhanced.



568

569 **Figure 11. (a)** Variation of MAE<sub>BC@870</sub> across cases of A–D, which correspond to the dust-  
 570 impacted, fire&dust-impacted, fire-impacted and typical samples, respectively. Results from the  
 571 typical samples were further divided into three subgroups, i.e., D-1 to D-3 which had SNA/EC ratios  
 572 of below 5, 5–10 and above 10, respectively. Comparisons of **(b)** RH and **(c)** SSA across D-1 to D-  
 573 3 (only the median values are shown).

#### 574 4. Conclusions

575 During a spring period with dramatic variations of PM<sub>2.5</sub> sources, PAX, AE33 and off-line  
 576 observations were integrated to explore the aerosol optical properties in a representative megacity  
 577 in Northeast China. PAX was used as the reference method to constrain the **multiple-scattering effect**  
 578 **scattering-associated artifacts** in the AE33-based absorption measurement. The correction factor  
 579 retrieved ( $C^*$ ) was found to depend positively on SSA whereas their relationship was non-linear. To  
 580 enhance the relevance of the time-resolved correction factors to future studies, we determined the  
 581 median  $C^*$  for various SSA bins, which covered the typical SSA ranges encountered in ambient  
 582 conditions. After applying the SSA-dependent  $C^*$ , the corrected AE33 results were in reasonable

583 agreement with the PAX-based absorption coefficients. We also observed considerable differences  
584 but strong correlations between the AE33 and off-line absorption measurements. For the absorption  
585 coefficient of bulk aerosol, the carbon analyzer reported higher values than AE33, with  $(b_{\text{abs}})^{\#}$   
586 approximately 50% larger than  $(b_{\text{abs}})^{*}$ . This discrepancy was primarily attributed to the  
587 different filter materials used by the two instruments. In addition, for the absorption coefficient of  
588 brown carbon, results from the AE33 were  $\sim 1.4$  times higher than those obtained by the  
589 spectrophotometric measurement of BrC solutions. A likely cause for this discrepancy was the  
590 difference in the states of the measured BrC (particulate vs. dissolved), while another contributor  
591 was inferred to be the chromophores insoluble in methanol, which were not accounted for in the  
592 solution-based approach.

593 After elucidating the relationships between the optical parameters determined by different  
594 approaches, we identified three types of episodes (i.e., dust-impacted, fire&dust-impacted, and fire-  
595 impacted) and the typical periods for the spring campaign. The classification was based on a  
596 synthesis of various signatures, including the MAE of BrC, the  $\text{PM}_{2.5}$  to  $\text{PM}_{10}$  ratio, wind speed and  
597 the  $\text{K}^+$  to sulfate ratio. The classification results were also supported by another two signatures,  
598  $\Delta\text{AAE}_{\text{BrC}}$  and  $E_{250}/E_{365}$ .

599 By comparing results from different periods, we highlighted the strong impacts of agricultural  
600 fire emissions on BrC. For example, the fires effectively enhanced the light absorption capacity of  
601 bulk BrC, emitted distinct chromophores with a characteristic absorption peak at  $\sim 365$  nm (as  
602 indicated by the increased  $\Delta\text{AAE}_{\text{BrC}}$ ), and produced organic compounds with relatively high  
603 molecular weights and aromatic contents (as indicated by the decreased  $E_{250}/E_{365}$ ). In addition, the  
604 agricultural fires, especially those having relatively low combustion efficiencies, effectively

605 increased the AAE of bulk aerosol and the BrC contribution to total absorption in the ultraviolet  
606 wavelength range.

607 We also unfolded the responses of BrC and BC optical properties to secondary aerosol  
608 formation. For typical samples, i.e., those without significant impacts from agricultural fires or dusts,  
609 we found that with the enhancement of secondary aerosol, the bulk BrC appeared less absorbing  
610 and consequently, the BrC influences on the light absorption of total aerosol became weaker, as  
611 reflected by the concurrent decreases in  $AAE_{\text{bulk}}$  and  $f_{\text{BrC}@370}$ . However, there was observational  
612 evidence pointing to a considerable increase in the MAE of BC driven by secondary aerosol  
613 production, which could be translated into ~~light absorption enhancement~~ ( $E_{\text{abs}}$ ) factors of up to ~2.3.

614 Finally, our results revealed the distinctiveness of the low-efficiency agricultural fire emissions  
615 in Northeast China. In addition to emitting unique organic matters (e.g., those with relatively high  
616 molecular weights and aromatic contents, and those strongly interfering thermal-optical EC  
617 determination), and effectively enhancing the BrC impacts on total aerosol light absorption, such  
618 fires could also promote nocturnal nitrate formation, likely due to some distinct dark-reactions. We  
619 suggest that the low-efficiency fires merit further investigations, e.g., for the emissions of gaseous  
620 and particulate species, the plume evolution, and the interactions of the fire emissions with other  
621 anthropogenic pollutants.

622 **Data availability.** Data described in this manuscript can be accessed at  
623 <https://doi.org/10.5281/zenodo.18898994> (Cheng, 2026).

624 **Author contributions.** YC and JL designed the study and prepared the paper, with inputs from all  
625 the co-authors. XC, YG, YZ and ZZ carried out the experiments. KH validated the results and  
626 supervised the study.

627 **Competing interests.** The authors declare that they have no conflict of interest.

628 **Disclaimer.** Publisher's note: Copernicus Publications remains neutral with regard to jurisdictional  
629 claims made in the text, published maps, institutional affiliations, or any other geographical  
630 representation in this paper. While Copernicus Publications makes every effort to include  
631 appropriate place names, the final responsibility lies with the authors.

632 **Acknowledgments.** The authors thank Dr. Yue-mei Han at Institute of Earth Environment, Chinese  
633 Academy of Sciences for the help in sample analysis.

634 **Financial support.** This research has been supported by the Jing-Jin-Ji Regional Integrated  
635 Environmental Improvement-National Science and Technology Major Project (2026ZD1216000),  
636 the National Natural Science Foundation of China (42222706), the Natural Science Foundation of  
637 Heilongjiang Province (YQ2024D011), and the Fundamental Research Funds for the Central  
638 Universities.

## 639 **References**

640 Adachi, K., Sedlacek III, A. J., Kleinman, L., Chand, D., Hubbe, J. M., and Buseck, P. R.: Volume  
641 changes upon heating of aerosol particles from biomass burning using transmission electron  
642 microscopy, *Aerosol Sci. Technol.*, 52, 46–56,  
643 <https://doi.org/10.1080/02786826.2017.1373181>, 2017.

644 Ahern, A. T., Goldberger, L., Jahl, L., Thornton, J., and Sullivan, R. C.: Production of N<sub>2</sub>O<sub>5</sub> and  
645 ClNO<sub>2</sub> through nocturnal processing of biomass-burning aerosol, *Environ. Sci. Technol.*, 52,  
646 550–559, <https://doi.org/10.1021/acs.est.7b04386>, 2018.

647 Anderson, L. D., Dix, B., Schnell, J., Yokelson, R., Veeffkind, J. P., Ahmadov, R., and de Gouw, J.:  
648 Analyzing the impact of evolving combustion conditions on the composition of wildfire  
649 emissions using satellite data, *Geophys. Res. Lett.*, 50, e2023GL105811,  
650 <https://doi.org/10.1029/2023GL105811>, 2023.

651 Andreae, M. O., and Gelencsér, A.: Black carbon or brown carbon? The nature of light-absorbing  
652 carbonaceous aerosols, *Atmos. Chem. Phys.*, 6, 3131–3148, [https://doi.org/10.5194/acp-6-](https://doi.org/10.5194/acp-6-3131-2006)  
653 3131-2006, 2006.

654 Atwi, K., Cheng, Z. Z., El Hajj, O., Perrie, C., and Saleh, R.: A dominant contribution to light  
655 absorption by methanol-insoluble brown carbon produced in the combustion of biomass fuels  
656 typically consumed in wildland fires in the United States, *Environ. Sci. Atmos.*, 2, 182–191,  
657 <https://doi.org/10.1039/d1ea00065a>, 2022.

658 Bi, X., Dai, Q., Wu, J., Zhang, Q., Zhang, W., Luo, R., Cheng, Y., Zhang, J., Wang, L., Yu, Z., Zhang,  
659 Y., Tian, Y., and Feng, Y.: Characteristics of the main primary source profiles of particulate  
660 matter across China from 1987 to 2017, *Atmos. Chem. Phys.*, 19, 3223–3243,  
661 <https://doi.org/10.5194/acp-19-3223-2019>, 2019.

662 Bond, T. C., Doherty, S. J., Fahey, D. W., Forster, P. M., Berntsen, T., DeAngelo, B. J., Flanner, M.  
663 G., Ghan, S., Kärcher, B., Koch, D., Kinne, S., Kondo, Y., Quinn, P. K., Sarofim, M. C., Schultz,  
664 M. G., Schulz, M., Venkataraman, C., Zhang, H., Zhang, S., Bellouin, N., Guttikunda, S. K.,  
665 Hopke, P. K., Jacobson, M. Z., Kaiser, J. W., Klimont, Z., Lohmann, U., Schwarz, J. P., Shindell,  
666 D., Storelvmo, T., Warren, S. G., and Zender, C. S.: Bounding the role of black carbon in the  
667 climate system: a scientific assessment, *J. Geophys. Res.*, 118, 5380–5552,  
668 <https://doi.org/10.1002/jgrd.50171>, 2013.

669 Cappa, C. D., Lim, C. Y., Hagan, D. H., Coggon, M., Koss, A., Sekimoto, K., de Gouw, J., Onasch,  
670 T. B., Warneke, C., and Kroll, J. H.: Biomass-burning-derived particles from a wide variety of  
671 fuels – Part 2: Effects of photochemical aging on particle optical and chemical properties,  
672 *Atmos. Chem. Phys.*, 20, 8511–8532, <https://doi.org/10.5194/acp-20-8511-2020>, 2020.

673 Chang, X., Zhao, B., Zheng, H. T., Wang, S. X., Cai, S. Y., Guo, F. Q., Gui, P., Huang, G. H., Wu,  
674 D., Han, L. C., Xing, J., Man, H. Y., Hu, R. L., Liang, C. R., Xu, Q. C., Qiu, X. H., Ding, D.,  
675 Liu, K. Y., Han, R., Robinson, A. L., and Donahue, N. M.: Full-volatility emission framework  
676 corrects missing and underestimated secondary organic aerosol sources, *One Earth*, 5, 403–  
677 412, 2022.

678 Chen, Q. C., Mu, Z., Song, W. H., Wang, Y. Q., Yang, Z. H., Zhang, L. X., and Zhang, Y. L.: Size-  
679 resolved characterization of the chromophores in atmospheric particulate matter from a typical

680 coal-burning city in China, *J. Geophys. Res. Atmos.*, 124, 10546–10563,  
681 <https://doi.org/10.1029/2019JD031149>, 2019.

682 Chen, X. Y., Ching, J., Wu, F., Matsui, H., Jacobson, M. Z., Zhang, F., Wang, Y. Y., Zhang, Z. X.,  
683 Liu, D. T., Zhu, S. P., Rudich, Y., Shi, Z. B., Yoo, H., Jeon, K. J., and Li, W. J.: Locating the  
684 missing absorption enhancement due to multi-core black carbon aerosols, *Nat. Commun.*, 16,  
685 10187, <https://doi.org/10.1038/s41467-025-65079-2>, 2025.

686 Cheng, Y.: Optical properties of carbonaceous aerosols modulated by source variations of spring  
687 haze, Zenodo [Data set], <https://doi.org/10.5281/zenodo.18898994>, 2026.

688 Cheng, Y., Cao, X. B., Liu, J. M., Zhong, Y. J., Yu, Q. Q., Zhang, Q., and He, K. B.: Measurement  
689 report: Diurnal variations of brown carbon during two distinct seasons in a megacity in  
690 northeast China, *Atmos. Chem. Phys.*, 23, 6241–6253, [https://doi.org/10.5194/acp-23-6241-](https://doi.org/10.5194/acp-23-6241-2023)  
691 2023, 2023.

692 Cheng, Y., and He, K. B.: Northeast China: an emerging hotspot of atmospheric sciences, *Sci. Bull.*,  
693 71, 64–66, <https://doi.org/10.1016/j.scib.2025.06.023>, 2026.

694 Cheng, Y., Yu, Q., Liu, J., Cao, X., Zhong, Y., Du, Z., Liang, L., Geng, G., Ma, W., Qi, H., Zhang,  
695 Q., and He, K.: Dramatic changes in Harbin aerosol during 2018–2020: the roles of open  
696 burning policy and secondary aerosol formation, *Atmos. Chem. Phys.*, 21, 15199–15211,  
697 <https://doi.org/10.5194/acp-21-15199-2021>, 2021.

698 Collaud Coen, M., Weingartner, E., Apituley, A., Ceburnis, D., Fierz-Schmidhauser, R., Flentje, H.,  
699 Henzing, J. S., Jennings, S. G., Moerman, M., Petzold, A., Schmid, O., and Baltensperger, U.:  
700 Minimizing light absorption measurement artifacts of the Aethalometer: evaluation of five  
701 correction algorithms, *Atmos. Meas. Tech.*, 3, 457–474, [https://doi.org/10.5194/amt-3-457-](https://doi.org/10.5194/amt-3-457-2010)  
702 2010, 2010.

703 Decker, Z. C. J., Zarzana, K. J., Coggon, M., Min, K. E., Pollack, I., Ryerson, T. B., Peischl, J.,  
704 Edwards, P., Dubé, W. P., Markovic, M. Z., Roberts, J. M., Veres, P. R., Graus, M., Warneke,  
705 C., de Gouw, J., Hatch, L. E., Barsanti, K. C., and Brown, S. S.: Nighttime chemical  
706 transformation in biomass burning plumes: a box model analysis initialized with aircraft  
707 observations, *Environ. Sci. Technol.*, 53, 2529–2538, <https://doi.org/10.1021/acs.est.8b05359>,  
708 2019.

709 Drinovec, L., Močnik, G., Zotter, P., Prévôt, A. S. H., Ruckstuhl, C., Coz, E., Rupakheti, M., Sciare,  
710 J., Müller, T., Wiedensohler, A., and Hansen, A. D. A.: The "dual-spot" Aethalometer: an  
711 improved measurement of aerosol black carbon with real-time loading compensation, *Atmos.*  
712 *Meas. Tech.*, 8, 1965–1979, <https://doi.org/10.5194/amt-8-1965-2015>, 2015.

713 Duarte, R. M. B. O., Pio, C. A., and Duarte, A. C.: Spectroscopic study of the water-soluble organic  
714 matter isolated from atmospheric aerosols collected under different atmospheric conditions,  
715 *Anal. Chim. Acta*, 530, 7–14, <https://doi.org/10.1016/j.aca.2004.08.049>, 2005.

716 Ferrero, L., Bernardoni, V., Santagostini, L., Cogliati, S., Soldan, F., Valentini, S., Massabò, D.,  
717 Močnik, G., Gregorič, A., Rigler, M., Prati, P., Bigogno, A., Losi, N., Valli, G., Vecchi, R., and  
718 Bolzacchini, E.: Consistent determination of the heating rate of light-absorbing aerosol using  
719 wavelength- and time-dependent Aethalometer multiple-scattering correction, *Sci. Total*  
720 *Environ.*, 791, 148277, <https://doi.org/10.1016/j.scitotenv.2021.148277>, 2021.

721 Gao, C. Y., Heald, C. L., Katich, J. M., Luo, G., and Yu, F. Q.: Remote aerosol simulated during the  
722 Atmospheric Tomography (ATom) campaign and implications for aerosol lifetime, *J. Geophys.*  
723 *Res. Atmos.*, 127, e2022JD036524, <https://doi.org/10.1029/2022JD036524>, 2022.

724 Geng, G. N., Liu, Y. X., Liu, Y., Liu, S. G., Cheng, J., Yan, L., Wu, N. N., Hu, H. W., Tong, D.,  
725 Zheng, B., Yin, Z. C., He, K. B., and Zhang, Q.: Efficacy of China's clean air actions to tackle  
726 PM<sub>2.5</sub> pollution between 2013 and 2020, *Nat. Geosci.*, 17, 987–994,  
727 <https://doi.org/10.1038/s41561-024-01540-z>, 2024.

728 Huang, X. F., Peng, Y., Wei, J., Peng, J. F., Lin, X. Y., Tang, M. X., Cheng, Y., Men, Z., Fang, T.,  
729 Zhang, J. S., He, L. Y., Cao, L. M., Liu, C., Zhang, C. C., Mao, H. J., Seinfeld, J. H., and Wang,  
730 Y.: Microphysical complexity of black carbon particles restricts their warming potential, *One*  
731 *Earth*, 7, 136–145, <https://doi.org/10.1016/j.oneear.2023.12.004>, 2024.

732 Karanasiou, A., Diapouli, E., Cavalli, F., Eleftheriadis, K., Viana, M., Alastuey, A., Querol, X., and  
733 Reche, C.: On the quantification of atmospheric carbonate carbon by thermal/optical analysis  
734 protocols, *Atmos. Meas. Tech.*, 4, 2409–2419, <https://doi.org/10.5194/amt-4-2409-2011>, 2011.

735 Kumar, N. K., Corbin, J. C., Bruns, E. A., Massabó, D., Slowik, J. G., Drinovec, L., Močnik, G.,  
736 Prati, P., Vlachou, A., Baltensperger, U., Gysel, M., El-Haddad, I., and Prévôt, A. S. H.:  
737 Production of particulate brown carbon during atmospheric aging of residential wood-burning

738 emissions, *Atmos. Chem. Phys.*, 18, 17843–17861, <https://doi.org/10.5194/acp-18-17843->  
739 2018, 2018.

740 Lack, D. A. and Langridge, J. M.: On the attribution of black and brown carbon light absorption  
741 using the Ångström exponent, *Atmos. Chem. Phys.*, 13, 10535–10543,  
742 <https://doi.org/10.5194/acp-13-10535-2013>, 2013.

743 Lambe, A. T., Cappa, C. D., Massoli, P., Onasch, T. B., Forestieri, S. D., Martin, A. T., Cummings,  
744 M. J., Croasdale, D. R., Brune, W. H., Worsnop, D. R., and Davidovits, P.: Relationship  
745 between oxidation level and optical properties of secondary organic aerosol, *Environ. Sci.*  
746 *Technol.*, 47, 6349–6357, <https://doi.org/10.1021/es401043j>, 2013.

747 Laskin, A., Laskin, J., and Nizkorodov, S. A.: Chemistry of atmospheric brown carbon, *Chem. Rev.*,  
748 115, 4335–4382, <https://doi.org/10.1021/cr5006167>, 2015.

749 Laskin, A., West, C. P., and Hettiyadura A. P. S.: Molecular insights into the composition, sources,  
750 and aging of atmospheric brown carbon, *Chem. Soc. Rev.*, 54, 1583,  
751 <https://doi.org/10.1039/d3cs00609c>, 2025.

752 Liu, J., Bergin, M., Guo, H., King, L., Kotra, N., Edgerton, E., and Weber, R. J.: Size-resolved  
753 measurements of brown carbon in water and methanol extracts and estimates of their  
754 contribution to ambient fine-particle light absorption, *Atmos. Chem. Phys.*, 13, 12389–12404,  
755 <https://doi.org/10.5194/acp-13-12389-2013>, 2013.

756 Liu, J., Lin, P., Laskin, A., Laskin, J., Kathmann, S. M., Wise, M., Caylor, R., Imholt, F., Selimovic,  
757 V., and Shilling, J. E.: Optical properties and aging of light-absorbing secondary organic  
758 aerosol, *Atmos. Chem. Phys.*, 16, 12815–12827, <https://doi.org/10.5194/acp-16-12815-2016>,  
759 2016.

760 Liu, S., Aiken, A. C., Gorkowski, K., Dubey, M. K., Cappa, C. D., Williams, L. R., Herndon, S. C.,  
761 Massoli, P., Fortner, E. C., Chhabra, P. S., Brooks, W. A., Onasch, T. B., Jayne, J. T., Worsnop,  
762 D. R., China, S., Sharma, N., Mazzoleni, C., Xu, L., Ng, N. L., Liu, D., Allan, J. D., Lee, J. D.,  
763 Fleming, Z. L., Mohr, C., Zotter, P., Szidat, S., and Prévôt, A. S. H.: Enhanced light absorption  
764 by mixed source black and brown carbon particles in UK winter, *Nat. Commun.*, 6, 8435,  
765 <https://doi.org/10.1038/ncomms9435>, 2014.

766 MEE (Ministry of Ecology and Environment of China): Ambient air quality standards (GB  
767 3095–2026), [https://www.mee.gov.cn/ywgf/fgbz/bz/bzwb/dqjhjbh/dqjhjzlbz/202602/t202602](https://www.mee.gov.cn/ywgf/fgbz/bz/bzwb/dqjhjbh/dqjhjzlbz/202602/t20260225_1144419.shtml)  
768 [25\\_1144419.shtml](https://www.mee.gov.cn/ywgf/fgbz/bz/bzwb/dqjhjbh/dqjhjzlbz/202602/t20260225_1144419.shtml), 2026.

769 Mo, Y., Li, J., Zhong, G., Zhu, S., Zhao, S., Tang, J., Jiang, H., Cheng, Z., Tian, C., Chen, Y., and  
770 Zhang, G.: The water-insoluble organic carbon in PM<sub>2.5</sub> of typical Chinese urban areas: light-  
771 absorbing properties, potential sources, radiative forcing effects, and a possible light-absorbing  
772 continuum, *Atmos. Chem. Phys.*, 24, 7755–7772, <https://doi.org/10.5194/acp-24-7755-2024>,  
773 2024.

774 ~~National Public Service Platform for Standards Information, Ambient Air Quality Standards,~~  
775 ~~<https://std.samr.gov.cn/gb/search/gbDetailed?id=4348B721E78BA160E06397BE0A0A32BA>,~~  
776 ~~2025.~~

777 Petzold, A., Ogren, J. A., Fiebig, M., Laj, P., Li, S. M., Baltensperger, U., Holzer-Popp, T., Kinne,  
778 S., Pappalardo, G., Sugimoto, N., Wehrli, C., Wiedensohler, A., and Zhang, X. Y.:  
779 Recommendations for reporting "black carbon" measurements, *Atmos. Chem. Phys.*, 13,  
780 8365–8379, <https://doi.org/10.5194/acp-13-8365-2013>, 2013.

781 Pileci, R. E., Modini, R. L., Bertò, M., Yuan, J., Corbin, J. C., Marinoni, A., Henzing, B., Moerman,  
782 M. M., Putaud, J. P., Spindler, G., Wehner, B., Müller, T., Tuch, T., Trentini, A., Zanatta, M.,  
783 Baltensperger, U., and Gysel-Beer, M.: Comparison of co-located refractory black carbon (rBC)  
784 and elemental carbon (EC) mass concentration measurements during field campaigns at several  
785 European sites, *Atmos. Meas. Tech.*, 14, 1379–1403, [https://doi.org/10.5194/amt-14-1379-](https://doi.org/10.5194/amt-14-1379-2021)  
786 2021, 2021.

787 Pöschl, U.: Atmospheric aerosols: composition, transformation, climate and health effects, *Angew.*  
788 *Chem. Int. Ed.*, 44, 7520–7540, <https://doi.org/10.1002/anie.200501122>, 2005.

789 Putaud, J. P., Cavalli, F., Yttri, K. E., Chow, J. C., Watson, J. G., Sinha, B., Venkataraman, C.,  
790 Ikemori, F., Jaffrezo, J. L., Uzu, G., Moreno, I., Krejci, R., Laj, P., Gupta, T., Hu, M., Kim, S.  
791 W., Mayol-Bracero, O., Quinn, P., Aas, W., Alastuey, A., Andrade, M., Angelucci, M., Anurag,  
792 G., Beukes, J. P., Bhardwaj, A., Chatterjee, A., Chaudhary, P., Chhangani, A. K., Conil, S.,  
793 Degorska, A., Devaliya, S., Dhandapani, A., Duhan, S. S., Dumka, U. C., Habib, G., Hamzavi,  
794 Z., Haswani, D., Herrmann, H., Holubova, A., Hueglin, C., Imran, M., Jehangir, A., Kapoor, T.  
795 S., Karanasiou, A., Khaiwal, R., Kim, J., Kolesa, T., Kozakiewicz, J., Kranjc, I., Laura, J. S.,

796 Lian, Y., Liu, J. W., Manwani, P., Mardoñez-Balderrama, V., Marticorena, B., Matsuki, A., Mor,  
797 S., Mukherjee, S., Murthy, S., Muthalagu, A., Najjar, T. A., Kumar, R. N., Pandithurai, G., Perez,  
798 N., Phairuang, W., Phuleria, H. C., Poulain, L., Prasad, L., Pullokaran, D., Qadri, A. M.,  
799 Qureshi, A., Ramírez, O., Roy, S., Rüdiger, J., Saikia, B. K., Saikia, P., Sauvage, S., Savvides,  
800 C., Sharma, R., Singh, T., Singh, G. K., Spoor, R., Srivastava, A. K., Raman, R. S., Van Zyl, P.  
801 G., Vecchiocattivi, M., Voiron, C., Xin, J. Y., and Yadav, K.: A worldwide aerosol  
802 phenomenology: elemental and organic carbon in PM<sub>2.5</sub> and PM<sub>10</sub>, *Atmos. Environ.*, 358,  
803 121338, <https://doi.org/10.1016/j.atmosenv.2025.121338>, 2025.

804 Putaud, J. P., Van Dingenen, R., Alastuey, A., Bauer, H., Birmili, W., Cyrys, J., Flentje, H., Fuzzi, S.,  
805 Gehrig, R., Hansson, H. C., Harrison, R. M., Herrmann, H., Hitzenberger, R., Hüglin, C., Jones,  
806 A. M., Kasper-Giebl, A., Kiss, G., Kousa, A., Kuhlbusch, T. A. J., Löschau, G., Maenhaut, W.,  
807 Molnar, A., Moreno, T., Pekkanen, J., Perrino, C., Pitz, M., Puxbaum, H., Querol, X.,  
808 Rodriguez, S., Salma, I., Schwarz, J., Smolik, J., Schneider, J., Spindler, G., ten Brink, H.,  
809 Tursic, J., Viana, M., Wiedensohler, A., and Raes, F.: A European aerosol phenomenology-3:  
810 Physical and chemical characteristics of particulate matter from 60 rural, urban, and kerbside  
811 sites across Europe, *Atmos. Environ.*, 44, 1308–1320, 2010.

812 Renzi, L., Di Biagio, C., Heuser, J., Zanatta, M., Cazaunau, M., Bergé, A., Panguì, E., Yon, J.,  
813 Isolabella, T., Massabò, D., Vernocchi, V., Mazzini, M., Vogel, F., Yu, C., Formenti, P., Picquet-  
814 Varrault, B., Doussin, J. F., and Marinoni, A.: The role of size in the multiple scattering  
815 correction C for dual-spot aethalometer: a field and laboratory investigation, *Atmos. Meas.*  
816 *Tech.*, 19, 1365–1383, <https://doi.org/10.5194/amt-19-1365-2026>, 2026.

817 Samset, B. H., Myhre, G., Herber, A., Kondo, Y., Li, S. M., Moteki, N., Koike, M., Oshima, N.,  
818 Schwarz, J. P., Balkanski, Y., Bauer, S. E., Bellouin, N., Berntsen, T. K., Bian, H., Chin, M.,  
819 Diehl, T., Easter, R. C., Ghan, S. J., Iversen, T., Kirkevåg, A., Lamarque, J. F., Lin, G., Liu, X.,  
820 Penner, J. E., Schulz, M., Seland, Ø., Skeie, R. B., Stier, P., Takemura, T., Tsigaridis, K., and  
821 Zhang, K.: Modelled black carbon radiative forcing and atmospheric lifetime in AeroCom  
822 Phase II constrained by aircraft observations, *Atmos. Chem. Phys.*, 14, 12465–12477,  
823 <https://doi.org/10.5194/acp-14-12465-2014>, 2014.

824 Sedlacek III, A. J., Buseck, P. R., Adachi, K., Onasch, T. B., Springston, S. R., and Kleinman, L.:  
825 Formation and evolution of tar balls from northwestern US wildfires, *Atmos. Chem. Phys.*, 18,  
826 11289–11301, <https://doi.org/10.5194/acp-18-11289-2018>, 2018.

827 Snyder, D. C., and Schauer, J. J.: An inter-comparison of two black carbon aerosol instruments and  
828 a semi-continuous elemental carbon instrument in the urban environment, *Aerosol Sci.*  
829 *Technol.*, 41, 463–474, <https://doi.org/10.1080/02786820701222819>, 2007.

830 Tinorua, S., Denjean, C., Nabat, P., Pont, V., Arnaud, M., Bourrienne, T., Dias Alves, M., and  
831 Gardrat, E.: A 2-year intercomparison of three methods for measuring black carbon  
832 concentration at a high-altitude research station in Europe, *Atmos. Meas. Tech.*, 17, 3897–3915,  
833 <https://doi.org/10.5194/amt-17-3897-2024>, 2024.

834 Tuccella, P., Di Antonio, L., Di Muzio, A., Colaiuda, V., Lidori, R., Menut, L., Pitari, G., and  
835 Raparelli, E.: Modeling the black and brown carbon absorption and their radiative impact: the  
836 June 2023 intense Canadian boreal wildfires case study, *J. Geophys. Res. Atmos.*, 130,  
837 e2024JD042674, <https://doi.org/10.1029/2024JD042674>, 2025.

838 van der Velde, I. R., van der Werf, G. R., Houweling, S., Eskes, H. J., Veefkind, J. P., Borsdorff, T.,  
839 and Aben, I.: Biomass burning combustion efficiency observed from space using  
840 measurements of CO and NO<sub>2</sub> by the TROPOspheric Monitoring Instrument (TROPOMI),  
841 *Atmos. Chem. Phys.*, 21, 597–616, <https://doi.org/10.5194/acp-21-597-2021>, 2021.

842 Wang, Y. Y., Zheng, Z. H., Sun, Y., Yao, Y., Ma, P. L., Zhang, A. X., ; Zhu, S. P., Zhang, Z. X., Chen,  
843 X. Y., Pang, Y. E., Wang, Q. Y., Che, H. Z., Ching, J., and Li, W. J.: Improved representation  
844 of black carbon mixing structures suggests stronger direct radiative heating, *One Earth*, 8,  
845 101311, <https://doi.org/10.1016/j.oneear.2025.101311>, 2025.

846 Washenfelder, R. A., Attwood, A. R., Brock, C. A., Guo, H., Xu, L., Weber, R. J., Ng, N. L., Allen,  
847 H. M., Ayres, B. R., Baumann, K., Cohen, R. C., Draper, D. C., Duffey, K. C., Edgerton, E.,  
848 Fry, J. L., Hu, W. W., Jimenez, J. L., Palm, B. B., Romer, P., Stone, E. A., Wooldridge, P. J.,  
849 and Brown, S. S.: Biomass burning dominates brown carbon absorption in the rural  
850 southeastern United States, *Geophys. Res. Lett.*, 42, 653–664,  
851 <https://doi.org/10.1002/2014GL062444>, 2015.

852 Weingartner, E., Saathoff, H., Schnaiter, M., Streit, N., Bitnar, B., and Baltensperger, U.: Absorption  
853 of light by soot particles: determination of the absorption coefficient by means of aethalometers,  
854 *J. Aerosol Sci.*, 34, 1445–1463, [https://doi.org/10.1016/S0021-8502\(03\)00359-8](https://doi.org/10.1016/S0021-8502(03)00359-8), 2003.

855 Winiger, P., Barrett, T. E., Sheesley, R. J., Huang, L., Sharma, S., Barrie, L. A., Yttri, K. E.,  
856 Evangeliou, N., Eckhardt, S., Stohl, A., Klimont, Z., Heyes, C., Semiletov, I. P., Dudarev, O.  
857 V., Charkin, A., Shakhova, N., Holmstrand, H., Andersson, A., and Gustafsson, Ö.: Source  
858 apportionment of circum-Arctic atmospheric black carbon from isotopes and modeling, *Sci.*  
859 *Adv.*, 5, eaau8052, <https://doi.org/10.1126/sciadv.aau8052>, 2019.

860 Wu, X., Cao, F., Haque, M., Fan, M. Y., Zhang, S. C., and Zhang, Y. L.: Molecular composition and  
861 source apportionment of fine organic aerosols in Northeast China, *Atmos. Environ.*, 239,  
862 117722, <https://doi.org/10.1016/j.atmosenv.2020.117722>, 2020.

863 Xiao, Q. Y., Geng, G. N., Xue, T., Liu, S. G., Cai, C. L., He, K. B., and Zhang, Q.: Tracking PM<sub>2.5</sub>  
864 and O<sub>3</sub> pollution and the related health burden in China 2013–2020, *Environ. Sci. Technol.*,  
865 56, 6922–6932, <https://doi.org/10.1021/acs.est.1c04548>, 2022.

866 Xie, X. C., Zhang, Y. Z., Liang, R. S., Chen, W., Zhang, P. X., Wang, X., Zhou, Y., Cheng, Y., and  
867 Liu, J. M.: Wintertime heavy haze episodes in Northeast China driven by agricultural fire  
868 emissions, *Environ. Sci. Tech. Lett.*, 11, 150–157, <https://doi.org/10.1021/acs.estlett.3c00940>,  
869 2024.

870 Yus-Diez, J., Bernardoni, V., Močnik, G., Alastuey, A., Ciniglia, D., Ivančič, M., Querol, X., Perez,  
871 N., Reche, C., Rigler, M., Vecchi, R., Valentini, S., and Pandolfi, M.: Determination of the  
872 multiple-scattering correction factor and its cross-sensitivity to scattering and wavelength  
873 dependence for different AE33 Aethalometer filter tapes: a multi-instrumental approach,  
874 *Atmos. Meas. Tech.*, 14, 6335–6355, <https://doi.org/10.5194/amt-14-6335-2021>, 2021.

875 Yus-Diez, J., Drinovec, L., Alados-Arboledas, L., Titos, G., Bazo, E., Casans, A., Patrón, D., Querol,  
876 X., Gonzalez-Romero, A., Perez García-Pando, C., and Močnik, G.: Characterization of filter  
877 photometer artifacts in soot and dust measurements – laboratory and ambient experiments  
878 using a traceably calibrated aerosol absorption reference, *Atmos. Meas. Tech.*, 18, 3073–3093,  
879 <https://doi.org/10.5194/amt-18-3073-2025>, 2025.

880 Zhang, J., Liu, L., Xu, L., Lin, Q., Zhao, H., Wang, Z., Guo, S., Hu, M., Liu, D., Shi, Z., Huang, D.,  
881 and Li, W.: Exploring wintertime regional haze in northeast China: role of coal and biomass

882 burning, *Atmos. Chem. Phys.*, 20, 5355–5372, <https://doi.org/10.5194/acp-20-5355-2020>,  
883 2020.

884 Zhang, X. L., Lin, Y. H., Surratt, J. D., Zotter, P., Prévôt, A. S. H., and Weber, R. J.: Light-absorbing  
885 soluble organic aerosol in Los Angeles and Atlanta: a contrast in secondary organic aerosol,  
886 *Geophys. Res. Lett.*, 38, L21810, <https://doi.org/10.1029/2011GL049385>, 2011.

887 Zhong, Q. R., Schutgens, N., van der Werf, G. R., Takemura, T., van Noije, T., Mielonen, T., Checa-  
888 Garcia, R., Lohmann, U., Kirkevåg, A., Olivie, D. J. L., Kokkola, H., Matsui, H., Kipling, Z.,  
889 Ginoux, P., Le Sager, P., Rémy, S., Bian, H. S., Chin, M., Zhang, K., Bauer, S. E., and Tsigaridis,  
890 K.: Threefold reduction of modeled uncertainty in direct radiative effects over biomass burning  
891 regions by constraining absorbing aerosols, *Sci. Adv.*, 9, eadi3568,  
892 <https://doi.org/10.1126/sciadv.adi3568>, 2023.